ADVANCED MATERIALS INTERFACES
Open Access
www.advmatinterfaces.de

Guidelines for Impedance Analysis of Parent Metal Anodes in Solid-State Batteries and the Role of Current Constriction at Interface Voids, Heterogeneities, and SEI

Janis K. Eckhardt, Till Fuchs, Simon Burkhardt, Peter J. Klar, Jürgen Janek, and Christian Heiliger*

Impedance spectroscopy is widely used in operando studies of solid-state batteries for characterizing charge transport and correlating it with structural features. A typical impedance spectrum reveals, in addition to transport signals of the solid electrolyte, one or more contributions due to processes taking place at the electrode interfaces. The focus of this study is on reversible (parent) metal anodes and a 3D electric network model is used to analyze the variation of their impedance as a function of pressure, temperature, or aging during cycling. This provides a recipe for experimentalists on how to identify impedance contributions arising from different interface effects, such as, charge transfer, dynamic current constriction, and solid electrolyte interphase formation. Rules are derived for assigning the different interface signals or identifying the dominant contribution in case of similar frequency-dependence and a standard procedure for analysis is proposed. The suggested procedure is applied to experimental data of half cells where lithium metal is in contact with garnet-type $Li_{6.25}Al_{0.25}La_3Zr_2O_{12}$. This case study yields unambiguously that geometric current constriction due to morphological instabilities at the metal anode interface during cycling is the rate-limiting step for this type of metal anode, rather than the frequently assumed polarization resistance of the electric charge transfer migration process.

1. Introduction

Electrochemical energy storage devices become increasingly important in the view of the growing share of renewable energy sources in power generation. The successful implementation of the parent metal anode in secondary batteries can be considered a new milestone in the development of novel or improved battery technologies with higher energy densities and lifetimes.[1–3] By replacing graphite, the currently most widespread anode material, with lithium, the theoretical specific capacity on the anode side can be increased by approximately a factor of 10. However, the side reactions occurring due to the high reactivity of alkali metals in general result in severe challenges.[4–6] Dendrites can lead to short circuits and, together with liquid electrolytes, to fires.[7–9] A major research focus is on the substitution of the common liquid electrolyte by a solid electrolyte (SE) in order to suppress the growth of dendrites, on the one hand, and to reduce the flammability of the batteries, on the other hand. SEs are applied as both separators and catholyte components in all-solid state battery systems. However, the chemical, kinetic and thermodynamic stability of the metal anode|SE interface, in particular, poses a major challenge in the development process.

In this study, we focus on the separator SE that will be in direct contact with the alkali metal. Several inorganic SE ceramics are not chemically stable against the respective alkali metal, which can lead to the formation of a resistive solid electrolyte interphase (SEI) that strongly affects the electric transport properties of the battery cell. For example, the

J. K. Eckhardt, C. Heiliger
Institute for Theoretical Physics
Justus Liebig University
Heinrich-Buff-Ring 16, D-35392 Giessen, Germany
E-mail: janis.k.eckhardt@theo.physik.uni-giessen.de

The ORCID identification number(s) for the author(s) of this article can be found under https://doi.org/10.1002/admi.202202354.

DOI: 10.1002/admi.202202354

J. K. Eckhardt, T. Fuchs, S. Burkhardt, P. J. Klar, J. Janek, C. Heiliger
Center for Materials Research (ZfM)
Justus Liebig University
Heinrich-Buff-Ring 16, D-35392 Giessen, Germany
T. Fuchs, S. Burkhardt, J. Janek
Institute of Physical Chemistry
Justus Liebig University
Heinrich-Buff-Ring 17, D-35392 Giessen, Germany
P. J. Klar
Institute of Experimental Physics I
Justus Liebig University
Heinrich-Buff-Ring 16, D-35392 Giessen, Germany

phenomenon of SEI formation plays a major role in argyrodite-type SEs versus lithium metal or sulfide-like variants of Na_3PS_4 versus sodium metal.[10–16] In addition, the mechanical properties of the solid materials involved have a major impact on the battery cells' performance. Unlike in the case of liquid electrolytes, a complicated interface morphology arises, when two solids come into mechanical contact. The contact formation depends, for example, on contact pressure, surface roughness, and the corresponding hardness of both materials. This can lead to the formation of pores of different shapes, sizes and depths at the interface. Similar interface morphologies occur upon plating or stripping of the metal electrode and the corresponding formation or annihilation of lattice defects, as originally suggested by Janek et al.[17–19]

Impedance spectroscopy (IS) is particularly suited for monitoring changes at the alkali metal|SE interface during operation due to comparably short measurement times. Individual contributions originating from microscopic transport processes within the SE (e.g., transport through the bulk of grains or across grain boundaries (GB)) may be separated from interface signals, if they differ in their characteristic time constants. The measured impedance data is mostly analyzed using 1D equivalent circuit models, although the actual transport through the real system is typically multidimensional and frequency-dependent.[20–22] As a result, this simplified analysis impedes a clear correlation between the macroscopic impedance response and microscopic transport processes, as mesoscopic phenomena such as dynamic current constriction (Cstr) due to the sample's morphology cannot be grabbed adequately.[23]

Nevertheless, experimental impedance data provide a powerful tool to correlate transport and structural properties and thus for operando monitoring of morphological changes, for example, at the interface between metal anode and solid electrolyte. Such impedance spectra exhibit one or more signals due to the interface. Recipes for experimentalists to assign the characteristics of these interface signals to the chemical and structural properties of the interface and the microscopic and mesoscopic transport processes across the interface are currently lacking. In the literature, the interface impedance is often simply attributed to an electric charge transfer (CT) process or SEI formation in the case of chemically unstable interfaces. Other processes that may become rate-limiting, such as diffusion of the reduced/oxidized species in the interface region, are only rarely considered.

Another important geometric effect that may affect the interface impedance is dynamic current constriction. In the case of reversible metal anodes under anodic current load (i.e., stripping), the accumulation of metal vacancies causes pore formation at the interface. This leads to a shrinkage of the electrochemically active surface area and an altering of the electrical and electrochemical properties.[24–28] Recent theoretical studies by Eckhardt et al.[29–30] and earlier work of Maier and Fleig[31–36] demonstrated that such pores lead to an additional geometric constriction resistance. Interestingly, the constriction effect can give rise to a separate semicircle in the Nyquist representation of the impedance data, resulting in a fingerprint that resembles a microscopic electric migration process. The corresponding impedance contribution, however, is not a microscopic transport process, but rather a global effect, which involves basically all the different microscopic transport processes occurring at the interface and adjacent regions.

The pore system is electrically insulating at low frequencies f of an exciting electric field, but it becomes dielectrically conductive at high frequencies. This change of conductivity with excitation frequency corresponds to a variation of the transport channels, where ions are injected into the SE. The whole electrode area and the entire SE volume can actively contribute to the transport through the system as long as pores at the interface are dielectrically conductive ($Z_{Pore} \approx 0\ \Omega$, displacement current). Insulating pores ($Z_{Pore} \rightarrow \infty\ \Omega$, electric current), however, lead to spatially focused (i.e., "constricted") ionic current lines at the remaining physical contact spots. The resulting constriction leads to a decrease of the active SE volume, which consequently causes a higher impedance.

SEI formation, CT between metal anode and SE or geometric current constriction, to name just a few possible reasons, are all effects related to the interface and contribute to the impedance response of the apparently reversible parent metal anode. In this study, we use a 3D electric network model to derive approaches, which allow experimentalists to analyze the interface impedance in terms of its origin and to identify the underlying microscopic process(es). For this purpose, the dependence of individual interface effects on stack pressure (i.e., contact area) and temperature are discussed. On this basis, we propose a novel approach and guideline for analyzing impedance data of electrode systems with chemically stable interfaces. This is validated by an experimental case study of a well-established system consisting of a lithium metal anode in contact with a garnet-type SE and corroborated by references to other published data. It reveals that current constriction due to morphological instabilities rather than the frequently assumed electric CT process is the rate-limiting step in the case of the system under study.

2. Computational Details

2.1. Description of the Model Structures

The 3D model systems considered comprise a dense polycrystalline solid electrolyte sandwiched between a metal working electrode (WE) and a metal counter electrode (CE) as shown in **Figure 1**a. The WE|SE interface is assumed to be non-ideal (e.g., porous), while an ideally-reversible and stable physical contact at the CE|SE interface is assumed serving as a quasi-reference electrode (QRE).[37] We assume a cubic shape of the SE ($L_x = L_y = L_z$) corresponding to a volume of $(100\ \mu m)^3$ and a thickness of 10 nm for the GBs including the adjacent space-charge region.[37–38] The non-ordered microstructure of the SE based on an average grain size of 10 µm is generated by using a Voronoi algorithm. We consider the same fixed typical microstructure of the SE in all series of simulations performed, where the relative physical contact area $A_{WE|SE} = A_{WE}/A_{SE}$ between WE and SE is varied. This enables a direct comparability of the computational results obtained for different materials parameters that can be assigned to interfaces, grains, and grain boundaries. It should be noted that the derived conclusions are general in nature and can also be applied to larger system sizes.

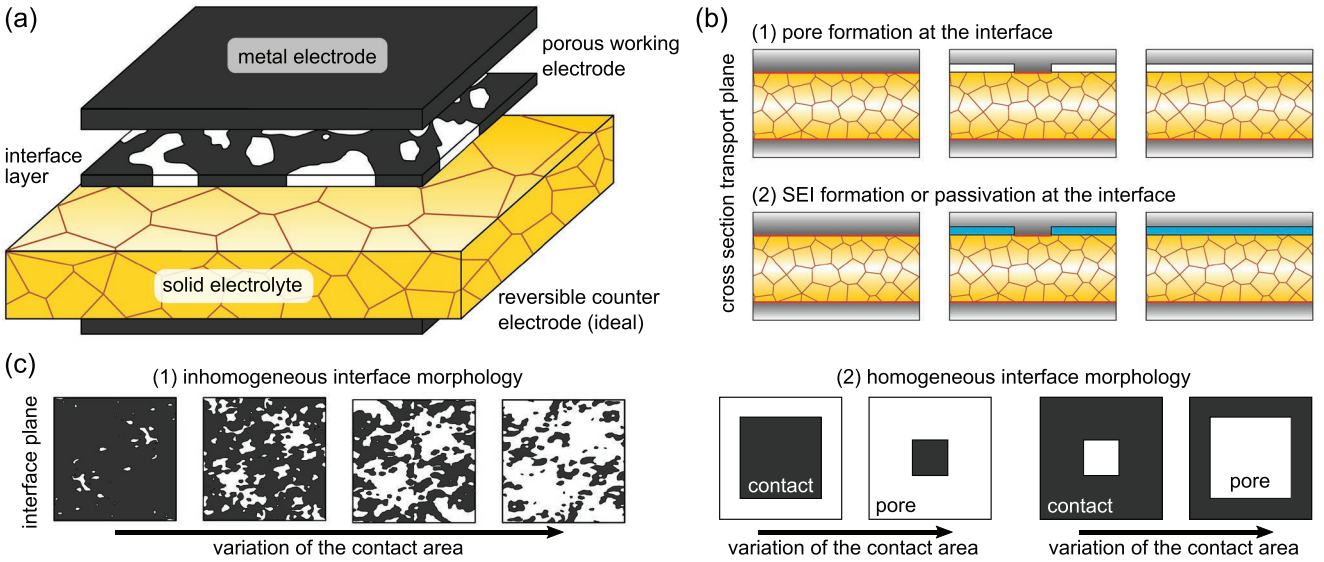

Figure 1. Schematic description of the 3D computational model systems. a) The cubic SE (yellow) is sandwiched between two metal electrodes (dark gray). The non-ideal WE|SE interface morphology is described by a separate quasi-2D layer of constant thickness. b) The effect of (1) pores and (2) an SEI or passivation is systematically studied using an impedance network model. Pores (white) are modeled as local capacitors, while the SEI or passivation (light blue) is described by local *RC*-elements with large resistivity. c) Overview of different (1) inhomogeneous and (2) homogeneous interface morphologies investigated. The former are derived from stress maps based on a multi-scale, time-dependent, 3D contact model reported by Zhang et al. Adapted with permission.[39] Copyright 2020, Elsevier.

The number of geometric model parameters for describing the WE|SE interface morphology is strongly reduced by focusing on a quasi-2D layer of constant thickness δ_{Int}. The latter is set to 10^{-4} of the transport length L_z and kept constant throughout all studies. The effect of this parameter on the impedance is discussed elsewhere.[29] In each series of computations, the relative physical contact area $A_{WE|SE}$ is systematically varied in size from 100% describing an ideal contact to 0% assuming a complete loss of contact. Such a loss or degradation of physical contact in real samples results either from pores or resistive inclusions (see Figure 1b). Experimental information on the explicit interface morphology at the mesoscale is difficult to access. Therefore, we consider four realistic inhomogeneous morphologies derived from lithium-surface-stress maps based on a multi-scale, time-dependent, 3D contact model published by Zhang et al.[39] The reported rectangular stress maps at various stack pressures were digitized, binarized, discretized, and extended via translation and rotation considerations to fit the geometry of our cubic 3D model system (see Figure 1c). In addition, we use two simplified interface geometries for comparison, whose ratio A_{WE}/A_{SE} can be continuously varied between ideal contact and no contact. One consists of a single square-shaped contact spot, and the second of a frame-like contact structure.

2.2. Description of the 3D Impedance Network and Choice of Materials Parameters

We use our 3D electric network model developed to describe the ion transport throughout the system.[29–30] *RC*-elements represent the electric transport processes within the SE (i.e., bulk and GB transport) in the nodal network. The redox reaction either oxidizing Me^0 or reducing Me^+ ions at the alkali metal|SE interfaces (i.e., the CT step) is also described by an *RC*-element based on a polarization resistance R_{Pol} and a double-layer capacitance C_{DL}. The notation of both microscopic parameters results from the Butler-Volmer description of the charge transfer across an interface. The pores and resistive inclusions or passivation reducing the physical contact area $A_{WE|SE}$ are mimicked by a capacitor and a *RC*-element with a large resistivity, respectively. It should be noted that we do not consider low-frequency diffusion processes in the system. The transport within the lithium metal electrode is assumed to be resistance-free. The same holds true, without loss of generality, for the CT step at the QRE. A detailed description about setting up the 3D electric network model and computing an impedance spectrum is given in our previous studies.[23,29–30]

We used the standard formulas for resistors and plate capacitors to calculate the values of the local circuit elements in the different layers of the sample. We chose as specific transport parameters values matching the garnet-type solid electrolyte $Li_{6.25}Al_{0.25}La_3Zr_2O_{12}$ (LLZO). The relative permittivity was set to $\varepsilon_{Bulk} = \varepsilon_{GB} = 150$.[37,40–41] The bulk ($\sigma_{Bulk} = 0.46$ mS cm^{-1}, $E_{a,Bulk} = 0.34$ eV) and GB ($\sigma_{GB} = 5.97$ µS cm^{-1}, $E_{a,GB} = 0.43$ eV) conductivities at room temperature were determined from temperature-dependent measurements.[37] The polarization resistance R_{Pol} describing the CT between metal electrode and SE was assumed to be 0.5 Ω cm^2 ($E_{a,CT} = 0.43$ eV). Three different parameter pairs for the double-layer capacitance C_{DL} and the pore capacitance $\tilde{C}_{Pore}$ were assumed to ensure a specific order of the characteristic time constants of CT and dynamic constriction, i.e., (1.77 F cm^{-2}, 885 µF cm^{-2}) for $\tau_{Cstr} < \tau_{CT}$, (1771 µF cm^{-2}, 443 µF cm^{-2}) for $\tau_{Cstr} \approx \tau_{CT}$, and (177 µF cm^{-2}, 4425 µF cm^{-2}) for $\tau_{CT} < \tau_{Cstr}$. The area-specific resistance $\tilde{R}_{SEI}$ and capacitance $\tilde{C}_{SEI}$ of the resistive SEI at the interface were assumed to be 100 Ω cm^2 and 88 µF cm^{-2}, respectively. Note that the single interface parameters are not necessarily related to the Li|LLZO interface.

2.3. Analysis of the Experimental Impedance Data and the Computed Impedance Series

All impedance spectra, those derived by the 3D network modelling and those obtained experimentally for the case study, were analyzed in the frequency domain by fitting them with an 1D equivalent circuit model. It consists of four *RC*-elements connected in series representing bulk and GB transport within the SE, dynamic current constriction, and CT at the WE|SE interface. The resulting parameter pairs (R_i, C_i) with i = (Bulk, GB, Cstr, CT) represent the macroscopic quantities of the single transport effects. The theoretical and experimental impedance data were also evaluated in the time domain by performing a distribution of relaxation times (DRT) analysis. Both types of analyses were performed using the commercial software RelaxIS 3 (version 3.0.20.16, rhd instruments GmbH & Co. KG).

The computed series of impedance spectra based on the 3D electric network model are almost free of noise signals (see Figures 3–7). The Kramers–Kronig test yields negligible residuals in the order of 10^{-6}%.[42] Therefore, all data points originating from these simulations were considered in the impedance analysis process, and only a small regularization term was required in the calculation of each DRT.[43]

Frequency points below 200 Hz were excluded in the analysis of the experimental impedance data shown in Figure 9, since individual residuals, particularly of the imaginary part, were greater than 4% in the Kramers–Kronig test.[42] The same holds for frequency points above 0.2 MHz, since the high frequency impedance contribution is only partially recorded in the measurement range. The corresponding DRT were calculated using exclusively the real part of the impedance as the residuals are in the range of a few 0.1% only, indicating high quality of the data. No additional data points were generated by interpolation and the second derivative of the distribution function $\gamma(\tau)$ was used in the Tikhonov regularization problem.[43]

3. Results

3.1. Challenges in Interpreting Experimental Impedance Data

An experimental system for investigating reversible metal anodes consists at least of a three-layer stack comprising a parent metal electrode (e.g., Li, Na, Ag, etc.), a highly dense polycrystalline SE, and a counter electrode. Various transport processes are expected to occur in such systems, namely bulk transport and transport across GBs within the SE and, in addition, electric CT at the metal|SE interface. Furthermore, one must distinguish between electric CT at the metal|SEI|SE boundary and dielectric conduction across the metal|pore|SE interface. It is anticipated that several of these processes may be separated from each other by IS as they should possess a different dependence on frequency of the applied external electric field.[44] Bulk transport processes typically possess characteristic frequencies in the high frequency range (i.e., several MHz) and GB transport in the medium frequency range (i.e., several kHz) at room temperature. Interface contribution(s) are typically expected at lower frequencies.[44]

In general, the impedance response of all-solid systems is highly affected by the solid|solid interface geometry. **Figure 2** depicts a schematic decision tree, whose branches correlate different interface morphology scenarios with transport effects reflected in the impedance signal of the interface. It is meant as a guideline for identifying the process(es) that are likely to dominate the metal anode|SE interface impedance in a specific scenario. The effects accounted for are an electric CT step at the metal|SE interface, a resistive SEI or passivation, and geometric current constriction due to pores or inclusions. It should be noted that we do not consider other processes such as transport limitations within the metal electrode.

From top to bottom of the decision tree, we distinguish on the first level between chemically stable and unstable interfaces, on the second level between ideal ($A_{WE|SE}$ = 100%) and non-ideal physical contact ($A_{WE|SE}$ < 100%), and on the third level between morphologically stable and unstable interfaces at the mesoscopic scale. The anticipated interface effects for each branch of the decision tree are given at the bottom level. Apparently, only in a few cases one expects a single interface effect to be responsible for its impedance contribution (e.g., outer left branch). Additional constriction effects are frequently expected in the case of non-ideal physical contacts. In such situations, it is very important to identify the dominant interface process(es) that lead to an increase in impedance, since the strategies for improving the electric interface characteristics of a (battery) system depend on the dominant process.

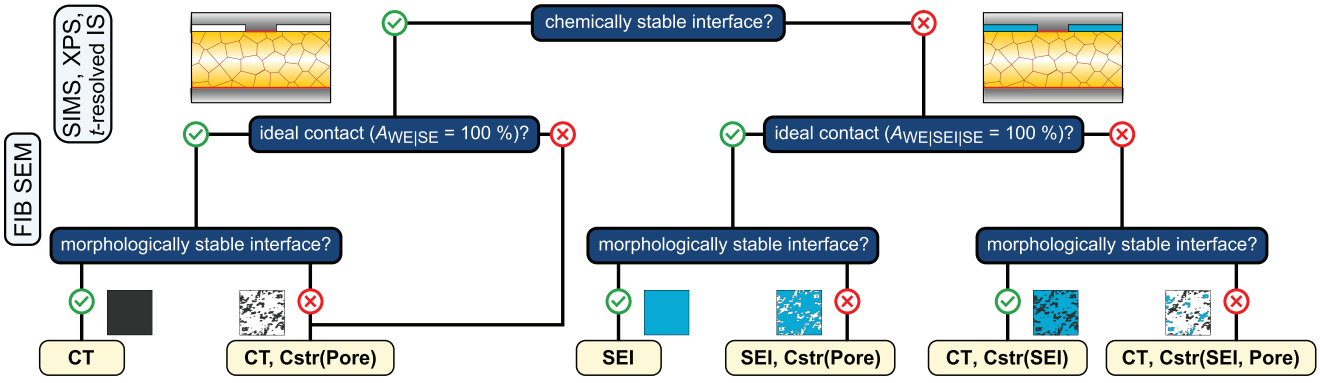

Figure 2. Effect of the geometric interface morphology on the impedance response of the system. The interface impedance in all-solid systems is often composed not only of electric migration processes, but also of additional geometric effects such as dynamic current constriction. Note that several other interface effects such as constriction due to transport limitations within the metal electrode are not considered in the decision tree.

For this purpose, measuring a single impedance spectrum of a sample and fitting it with a 1D equivalent circuit model is not sufficient. It cannot fully resolve the significance of different interface effects, since it does not lead to individual characteristic impedance features. Moreover, often only one impedance signal assigned to the interface is experimentally observed, although several processes contribute. Therefore, establishing the relevance of different interface effects typically requires additional experimental input. This can be obtained, for example, by systematic variation of external parameters and monitoring of their impact on the sample's impedance response. This comprises in particular, experiments where the stack pressure is varied and the pristine interface with $A_{WE|SE} < 100\%$ due to porosity or inclusions becomes almost ideal. Although such experiments cause irreversible changes of the sample's morphology, they allow to "switch off" current constriction effects. Similarly, temperature-dependent measurements yield activation energies of the macroscopic resistances extracted from the impedances accounted for in the 1D equivalent circuit model used for fitting the experimental impedance spectra. This is helpful, as the constriction resistance arises from an averaging of different microscopic electric migration processes at the interface.

Such comprehensive impedance studies need to be complemented by direct investigations of the interface morphology. The chemical stability of an interface can be studied by time-resolved IS measurements complemented by well-established methods such as X-ray photoelectron spectroscopy (XPS) or secondary-ion mass spectrometry (SIMS).[45–47] The quality of the physical contact and its morphological stability under operation can be probed using focused ion beam scanning electron microscopy (FIB SEM).[48–50] Combining all these efforts allows experimentalists to correlate changes of impedance spectra during cycling with degradation of the cell caused by morphology changes at the metal anode|SE interface. Thus, such studies are essential for optimizing all-solid-state batteries employing metal anodes in a systematic fashion.

3.2. Signatures of Various Interface Processes on the Impedance Response of Battery Systems

The charge transfer at the metal|SE interface, the successive formation of an SEI, passivation or pores at the interface, they all affect the interface characteristics in their own specific manner. To highlight their individual signatures in the impedance response of the system, series of impedance spectra are computed using a 3D electric network model. Throughout each series, we systematically vary the interface morphology of the model system as depicted in Figure 1 for a given set of materials parameters. The computed impedance spectra were subsequently analyzed with a 1D equivalent circuit model consisting of four *RC*-elements connected in series to derive the macroscopic transport parameters (R_i, C_i) of bulk and GB transport within the SE as well as CT and geometric constriction effects due to pores or SEI formation at the interface. It should be noted that assuming a constant interface thickness δ_{Int} throughout an impedance series may lead to an overestimation of the fit parameter $\tau_{Cstr} = R_{Cstr} \cdot C_{Cstr}$ in the computations compared to experimental observation, as the simultaneous decrease in δ_{Int} somewhat compensates the effect of a decreasing $A_{WE|SE}$.[29] In this section, we first systematically investigate the branch of chemically stable interfaces within the decision tree, i.e., assuming no SEI formation or passivation, and then address chemically unstable interfaces with SEI formation.

3.2.1. Effect of Morphological Instabilities Due to Pore Formation at Chemically Stable Interfaces

We assume an interface that is free of a passivation or resistive SEI layer in this subsection. Such a situation is, for example, experimentally observed for lithium metal in contact with a garnet-type SE.[51–54] In the modelling, we keep the microstructure of the SE constant, whilst varying the pore distribution at the WE|SE interface. We compare the computational results of the four realistic interface morphologies based on the multi-scale contact model[39] with two simplified interface morphologies consisting of one square-shaped contact spot and one frame-like contact structure whose lateral extensions can be varied continuously in size, as shown in Figure 1c. The macroscopic transport parameters (R_i, C_i) extracted from the modelled impedance spectra by the 1D fitting approach are analyzed with respect to their dependence on interface morphology, contact area, and temperature. Thereby, we consider three different pairs of parameters for the double-layer and pore capacitance (see Section 2) to explore the order of constriction and CT relaxation time on the scale of time constants, since τ_{Cstr} has a significant effect on the shape of the impedance spectrum and thus the derived conclusions.

Influence of Inhomogeneous Interface Morphologies: Each of the graphs depicted in **Figure 3**a–c shows five impedance spectra in Nyquist representation based on the disordered interface morphologies between WE and SE depicted on their right. The three graphs correspond to different orders of interface time constants, i.e., $\tau_{Cstr} < \tau_{CT}$, $\tau_{Cstr} \approx \tau_{CT}$, and $\tau_{CT} < \tau_{Cstr}$, respectively. The relative contact area $A_{WE|SE}$ in each computation series varies between 100% (bottom) and 22% (top). Three semicircles can be visually observed, when considering an ideal physical contact ($A_{WE|SE} = 100\%$). These correspond to the two ion migration processes within the SE and the CT step at the interface. Bulk and GB impedances corresponding to the blue and red semicircles, respectively, remain unchanged when reducing the contact area by pore formation. Pore formation lead to dynamic current constriction that occurs as an additional geometric effect in the spectrum, which affects the interface impedance. As a general trend, the DC resistance of the whole electrode system increases with decreasing $A_{WE|SE}$, as indicated by the shift of the outer impedance semicircle to the right. However, the interface response differs in detail for the three cases of order of τ_{Cstr} and τ_{CT}.

The order of the time constants determines how the morphological changes at the interface are reflected in the impedance spectrum. For $\tau_{Cstr} < \tau_{CT}$ shown in Figure 3a, the change in impedance is related to the formation of an additional geometric constriction semicircle (yellow) between that of the GB (red) and the CT signal (green). In addition, the CT impedance contribution (green) at lower frequencies simultaneously

ADVANCED MATERIALS INTERFACES
Open Access
www.advmatinterfaces.de

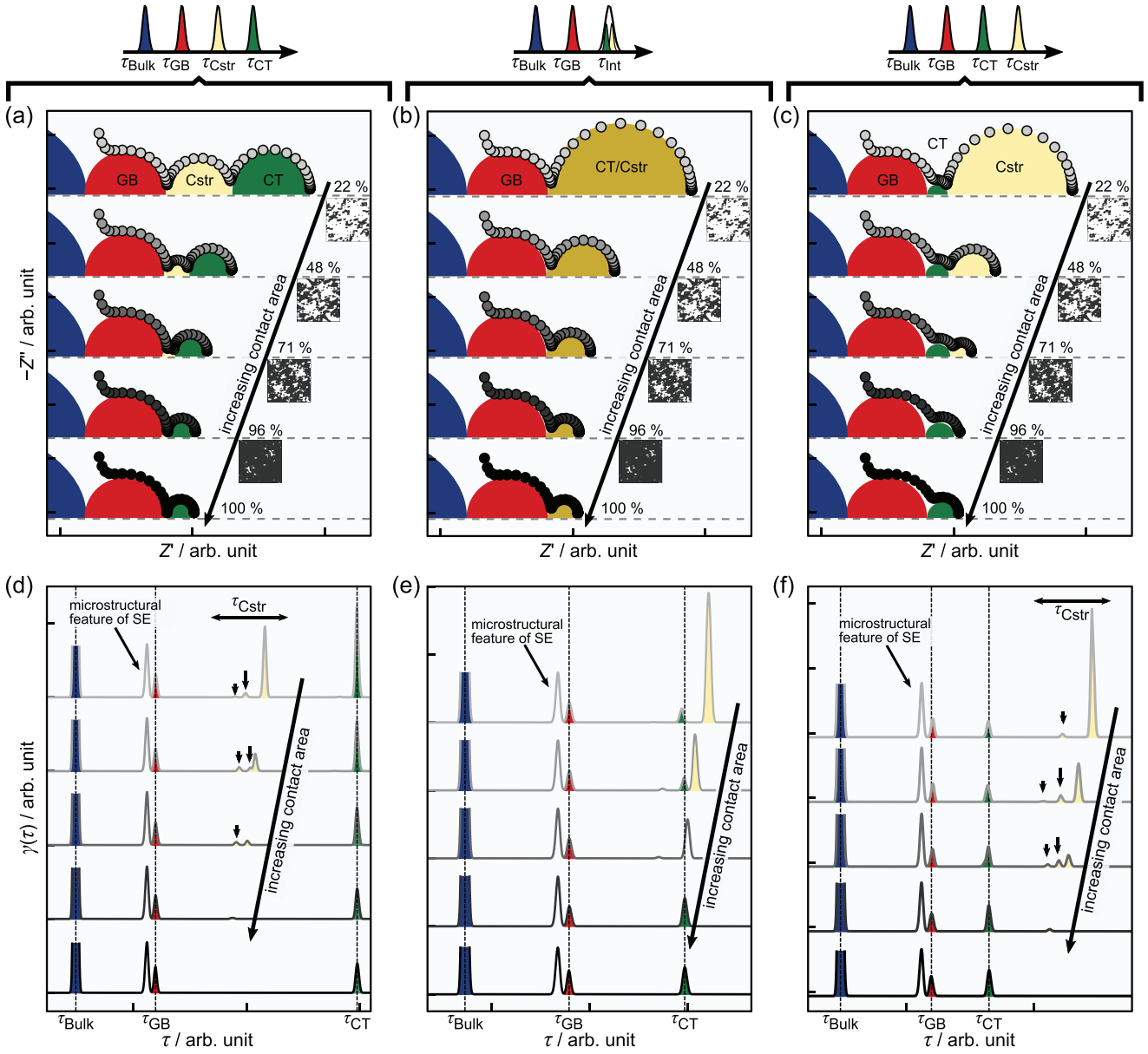

Figure 3. Computed series of impedance spectra in Nyquist representation and corresponding DRT analyses for various realistic WE|SE interface morphologies (inset) considering different orders of the time constants of CT and dynamic current constriction. The interface morphologies originate from simulated Li-surface-stress maps reported by Zhang et al. Adapted with permission.[39] Copyright 2020, Elsevier. Note that the bulk impedance (blue) is not fully displayed for clarity and low-frequency diffusion processes are not considered in the modeling. a–c) A porous interface leads to a constriction effect (yellow), which results in an increase in impedance with decreasing contact area $A_{WE|SE}$. The shape of the impedance and the changes of individual contributions depend on the order of the time constants of the interface processes involved. d–f) An inhomogeneous distribution of pores at the interface leads to additional DRT signals (black arrows) in the vicinity of the major constriction signal (yellow).

increases in size. In the case of similar time constants $\tau_{Cstr} \approx \tau_{CT}$ depicted in Figure 3b, only one effective interface semicircle (ochre) can be visually observed in the Nyquist representation of the impedance spectra that increases in size with decreasing $A_{WE|SE}$. In Figure 3c, where the order of time constants is reversed ($\tau_{CT} < \tau_{Cstr}$), an increasing geometric constriction semicircle (yellow) arises to the right of the CT signal (green) and dominates the interface impedance response with decreasing $A_{WE|SE}$, whilst the CT impedance decreases. It should be noted, however, that the DC resistance in the three cases is independent of the arrangement of the time constants for all $A_{WE|SE}$. This is not a universal effect, but is related to the modeling of the different order of time constants τ_i in the computations by adjusting the magnitude of the local capacitances in the 3D electric network, but not that of the local resistors. In the DC case ($f = 0$ Hz), the impedance of a local *RC*-element is solely given by its ohmic contribution. This is due to the fact that the capacitor is connected in parallel with a corresponding resistor and the absolute value of its impedance becomes infinity, i.e., $|Z_C(f = 0\ \text{Hz})| = \infty\ \Omega$.

To investigate the effects of structural disorder and order of the time constants in more detail, we performed DRT analyses of the three series of impedance data as depicted in Figure 3d–f. Here, the amplitude of the leftmost signal (blue) corresponding to the bulk transport has been truncated in all DRT for a clearer data representation. The DRT corresponding to an ideal contact ($A_{WE|SE}$ = 100%) consist of four signals independent of the order of the time constants. The center positions of three signals match the (input) time constants of the microscopic electric transport processes in the system, i.e., bulk (blue) and GB (red) transport in the SE, and CT (green) at the WE|SE interface. The fourth signal in the vicinity of the GB time constant is related to the inhomogeneous synthetic microstructure of the SE and results from competing transport paths through the system which yield slightly different time constants. The occurrence of this effect in inhomogeneous samples can be analytically proven as demonstrated in our previous work.[23]

In the case of $\tau_{Cstr} < \tau_{CT}$ shown in Figure 3d, several additional signals form in the intermediate time range between GB and CT relaxation time, when the contact area $A_{WE|SE}$ is reduced. The strong dependence of the time constants (central position of these signals on the relaxation time axis) on $A_{WE|SE}$, especially of the main signal, is a characteristic feature of their geometric origin. In comparison, the time constant of a microscopic or local electric migration process does not depend on $A_{WE|SE}$. The dependence of these signals on $A_{WE|SE}$ reflects that dynamic constriction is a global effect, which varies with the interface morphology and averages over the time constants of the microscopic processes within the system. The smaller geometric signals (indicated by black arrows in the graphs) result from the inhomogeneous spatial distribution and the different sizes of the pores, since penetration depth and constriction region (i.e., the region in which equipotential lines are not parallel to the interface) increase with pore size. This implies that not only a pore depth distribution[29] leads to a (strongly) distorted constriction impedance, but also an inhomogeneous interface morphology with a broad pore size distribution. Similar results were recently also observed experimentally.[55–56] This finding is independent of the order of time constants. The signals related to the disorder (black arrows) shift with τ_{Cstr}. Thus, they are difficult to resolve in the case of $\tau_{Cstr} \approx \tau_{CT}$, but they can be easily observed again when $\tau_{CT} < \tau_{Cstr}$.

We continue our analysis of the model results by extracting the macroscopic transport parameters (R_i, C_i) from the computed impedance spectra by fitting them with a 1D equivalent circuit model. **Figure 4**a–c shows the evolution of the charge transfer (R_{CT}, C_{CT}, τ_{CT}), effective interface (R_{Int}, C_{Int}, τ_{Int}), and dynamic constriction parameters (R_{Cstr}, C_{Cstr}, τ_{Cstr}) as a function of $A_{WE|SE}$ for the three cases of order of time constants τ_{CT} and τ_{Cstr}. In the analysis, we also considered two simplified interface geometries, i.e., a single contact spot (blue triangles) and a frame-like contact spot (yellow squares), where $A_{WE|SE}$ can be tuned continuously, in addition to the five realistic interface morphologies (red circles). The macroscopic bulk (R_{Bulk}) and GB transport parameters (R_{GB}) are given as horizontal reference lines in green and orange, respectively, since both do not depend on the pore fraction at the two-phase boundary $A_{WE|SE}$. The reference line of the geometric pore capacitance C_{Pore} is displayed in black.

In the case of $\tau_{Cstr} < \tau_{CT}$ depicted in Figure 4a, the CT and constriction resistances (R_{Cstr}, R_{CT}) increase with decreasing $A_{WE|SE}$. The constriction capacitance C_{Cstr} approaches that of the pores C_{Pore} and the CT capacitance C_{CT} decreases with decreasing contact area $A_{WE|SE}$. The time constant of the CT electric migration process is preserved, while that of geometric current constriction changes by about three orders of magnitude. The reason is that R_{Cstr} tends to infinity and the capacitance C_{Cstr} tends toward C_{Pore} when $A_{WE|SE}$ goes to zero, i.e., for complete loss of physical contact. The CT transport parameters (R_{CT}, C_{CT}) are almost unaffected by the distribution of the contact area at the interface for constant $A_{WE|SE}$, in contrast to the geometric constriction parameters (R_{Cstr}, C_{Cstr}). Especially the resistance R_{Cstr} is strongly affected by the morphology of the interface. Its sensitivity on the distribution of the physical contact for fixed $A_{WE|SE}$ increases with decreasing $A_{WE|SE}$. The value of R_{Cstr} is the lower, the finer the distribution of the physical contact is at the interface. The constriction capacitance, on the other hand, is not affected by the distribution of contact. This behavior is known and discussed in more detail in our previous work and also by Maier and Fleig.[29,33]

In the case of $\tau_{Cstr} \approx \tau_{CT}$, only one interface signal can be visually observed in the modelled impedance spectra. The corresponding macroscopic transport parameters (R_{Int}, C_{Int}) extracted by fitting with the 1D equivalent circuit model reflect the superposition of CT and constriction effects, as shown in Figure 4b. The electric CT migration process dominates for an ideal physical contact, but the impact of geometric constriction becomes more prominent with decreasing contact area. The magnitude of the effective resistance R_{Int} depends significantly on the interface morphology for small $A_{WE|SE}$ similar to R_{Cstr} in case of $\tau_{Cstr} < \tau_{CT}$ shown in Figure 4a. The effective capacitance C_{Int} converges towards a certain value and the time constant τ_{Int} increases by about 1.5 orders of magnitude with decreasing $A_{WE|SE}$. These findings clearly indicate that the impact of geometric constriction in the case of a single interface impedance signal is not negligible, in particular, when $A_{WE|SE}$ is smaller than 50%.

The qualitative behavior of the macroscopic CT parameters (R_{CT}, C_{CT}) changes drastically, when the order of time constants is reversed, i.e., $\tau_{CT} < \tau_{Cstr}$, whereas that of dynamic constriction (R_{Cstr}, C_{Cstr}) is only quantitatively affected. Figure 4c highlights that the CT resistance R_{CT} decreases and the CT capacitance C_{CT} increases with decreasing contact area $A_{WE|SE}$. The trends of these two macroscopic parameters with $A_{WE|SE}$ are opposite to those of the two cases shown in Figure 4a,b. The behavior is somewhat surprising at first glance, but it is related to different evolving transport paths through the system for frequencies close to $1/\tau_{CT}$. All transport channels are nearly perpendicular to the interface and parallel to each other, i.e., not constricted anymore, since the pores are dielectrically conductive in this frequency range.[30] This is discussed in more detail in the next section.

Functional Dependence of Charge Transfer and Constriction Resistance on the Contact Area: The distinction between CT and constriction impedance is simplified if both contributions are well-separated in the spectrum. This is usually not the case in experimental data, which may explain why different functional relationships of what is summed up as *interface resistance*

ADVANCED MATERIALS INTERFACES
Open Access
www.advmatinterfaces.de

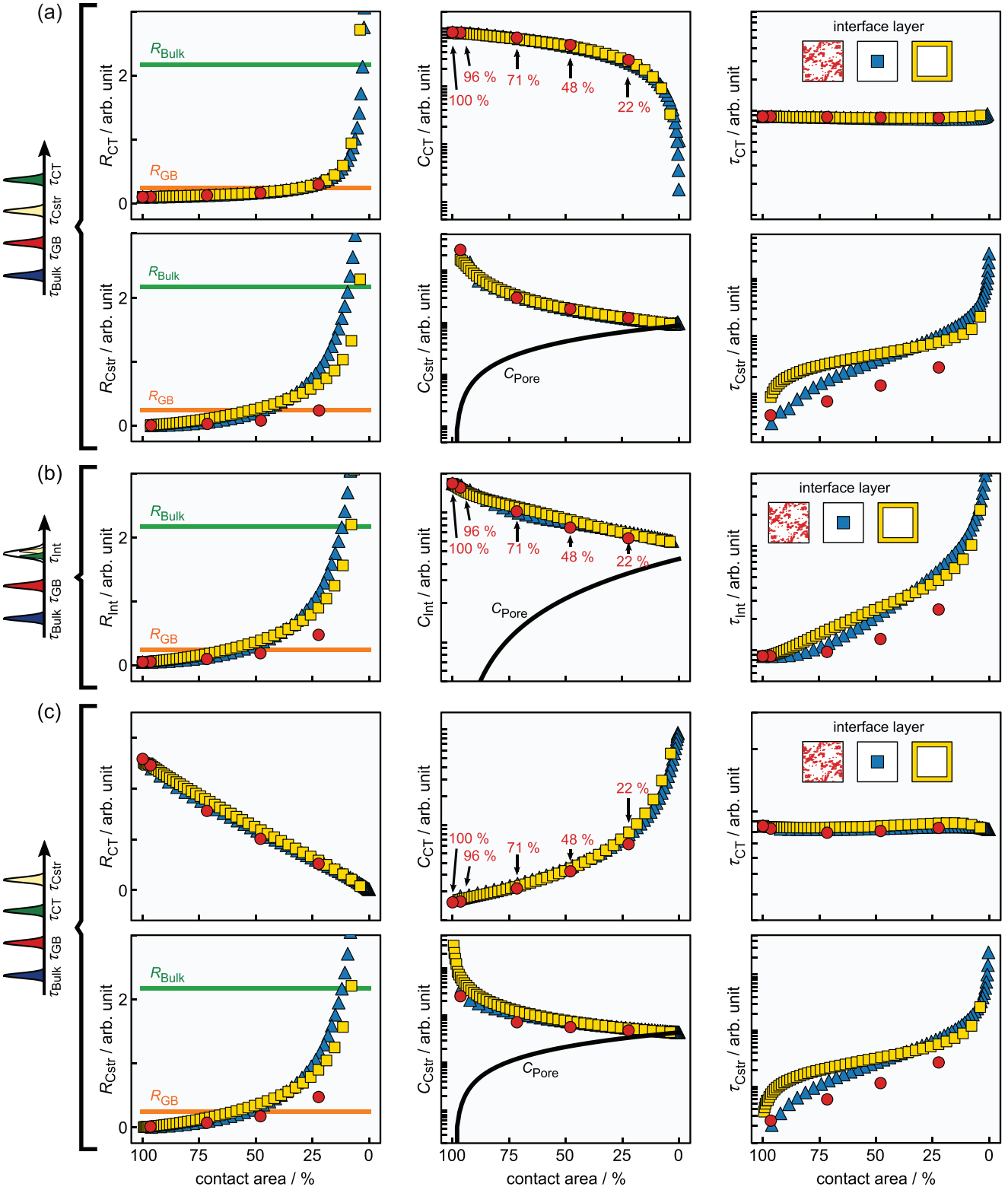

Figure 4. Evolution of the macroscopic transport parameters (R_i, C_i, τ_i) of the interface contributions, considering different orders of time constants, i.e., a) $\tau_{Cstr} < \tau_{CT}$, b) $\tau_{Cstr} \approx \tau_{CT}$, and c) $\tau_{CT} < \tau_{Cstr}$. The bulk (green) and GB (orange) parameters are independent of the pore fraction at the interface and shown as reference values. The CT parameters at constant contact area are nearly independent of the interface morphology but their qualitative behavior is not universal. It depends on the order of time constants. The constriction resistance, in contrast, depends on the distribution of the physical contact area at the interface.

under force application are discussed in the literature.[37,39] It is frequently ignored that the interface impedance can have different origins and therefore a different dependence of the corresponding resistance R_i and capacitance values C_i on external parameters, such as stack pressure. This underlines the need for a theoretical in-depth analysis in order to evaluate how the constriction parameters (R_{Cstr}, C_{Cstr}) and the CT parameters (R_{CT}, C_{CT}) of the interface impedance behave, when the physical contact area $A_{WE|SE}$ is varied. For this purpose, the macroscopic transport parameters of the three computed impedance series shown in Figure 4 considering different orders of time constants τ_{Cstr} and τ_{CT} are further analyzed using a double logarithmic data representation, i.e., log R_i versus log $A_{WE|SE}$ and log C_i versus log $A_{WE|SE}$. This kind of data evaluation only holds, if the QRE does not affect the derived CT parameters, i.e., $Z_{QRE} = 0\ \Omega$. Otherwise, the offset due to the QRE needs to be subtracted from the CT parameters prior to calculating log R_i and log C_i.

The constriction resistance R_{Cstr} in **Figure 5**a,f is not proportional to $A_{WE|SE}^{-1}$, i.e., it does not exhibit a slope of –1 in the double-logarithmic data representation log R_{Cstr} versus log $A_{WE|SE}$. Once the constriction signal can be resolved in the impedance spectrum, R_{Cstr} increases by several orders of magnitude and may also become significantly larger than R_{CT}. Starting from a constriction resistance of zero for an ideal interface contact ($A_{WE|SE} = 100\%$), there is a sharp non-linear increase of log R_{Cstr} as log $A_{WE|SE}$ decreases, followed by an almost linear subregion with lower resistance increases at small contact areas. The general behavior, however, depends on the combination of the geometric interface morphology, the phases present at the interface and the corresponding materials parameters. Nonetheless, the qualitative trends are independent of the order of the time constants, but the increase in constriction resistance R_{Cstr} is somewhat more pronounced in the case of $\tau_{CT} < \tau_{Cstr}$.

The finding that R_{Cstr} is not proportional to $A_{WE|SE}^{-1}$ reflects the mesoscopic character of the constriction phenomenon. The impact of a variation of the physical contact area $A_{WE|SE}$ is not restricted to the interface layer itself, but globally affects the transport paths taken by the charge carriers through the system. Therefore, geometric parameters, such as the distribution of the pores or physical contact have a major effect on the magnitude of R_{Cstr}.[29,33] This indicates that performing the same experiment in the laboratory several times on nominally identical samples will lead to a distribution of resistances R_{Cstr} due to non-reproducible interface morphologies (i.e., geometric differences on the mesoscale). The impact of the variation of the interface morphology on R_{Cstr} is particularly pronounced at small physical contact areas. In consequence, a variance in the corresponding experimental data is not necessarily due to uncertainty in the measurement or in the fitting process with a 1D equivalent circuit model. Instead, the variance may reflect a change of the interface morphology and, thus, be at least partially of geometric origin. Therefore, the measure of the impedance in applications may be used for health monitoring of the interface. If the same sample is measured several times, for example, repeatedly during cycling, and the resistance R_{Cstr} changes, it is an indicator that the interface degrades. However, no simple functional or analytical relation between constriction resistance and contact area $A_{WE|SE}$ exists, but these considerations underline again the importance of the structural information about the interface morphology.

We applied the same procedure to evaluate the functional relationship of the CT resistance R_{CT} and the CT capacitance C_{CT}. The double logarithmic data representation in Figure 5b for $\tau_{Cstr} < \tau_{CT}$ shows a nearly linear relation between log R_{CT} and log $A_{WE|SE}$ that is almost independent of the interface morphology. Fitting the data with a linear function reveals slopes in the range of –1.03 and –1.08 for the three model systems considering different interface morphologies. Similar results are observed for the CT capacitance C_{CT}, as shown in Figure 5c. It also depends linearly on the contact area with slopes between 1.02 and 1.08. Interestingly, the functional relationships of R_{CT} and C_{CT} show a very different behavior in the case of the reversed order of the time constants ($\tau_{CT} < \tau_{Cstr}$) as shown in Figure 5g,h, respectively. The data representations of log R_{CT} versus log $A_{WE|SE}$ now exhibit slopes of approximately +1 and those of log C_{CT} versus log $A_{WE|SE}$ slopes of about –1. In other words, the sign of the slopes in the case of resistance and capacitance is reversed with the order of the time constants.

At first glance, this finding is unexpected because CT is a microscopic electric migration process and, therefore, its impact should remain restricted to the interface, other than in the case of the mesoscopic constriction effect. The macroscopic CT resistance and capacitance are expected to be proportional to the inverse of the active interface area ($R_{CT} \sim A_{WE|SE}^{-1}$) and proportional to the active interface area itself ($C_{CT} \sim A_{WE|SE}$), respectively. The deviating observations from this behavior are related to the evolving transport paths through the system. In the case of $\tau_{Cstr} < \tau_{CT}$, the pores at the interface are insulating for frequencies when the CT impedance signal arises. Therefore, the active fraction of the interface corresponds to $A_{WE|SE}$. This is why $R_{CT} \sim A_{WE|SE}^{-1}$ and $C_{CT} \sim A_{WE|SE}$ with slopes of –1 and +1 for log R_{CT} versus log $A_{WE|SE}$ and log C_{CT} versus log $A_{WE|SE}$, respectively. The transport situation is changed when considering the reversed order of time constants $\tau_{CT} < \tau_{Cstr}$. The pores at the interface are dielectrically conductive in the frequency range of the CT impedance signal. If the conduction contribution across the pores is comparable to that across the physical contact spots, the current is homogeneously distributed across the interface. In this situation, the CT resistance will linearly decrease $R_{CT} \sim A_{WE|SE}$ and CT capacitance will increase $C_{CT} \sim A_{WE|SE}^{-1}$ with decreasing $A_{WE|SE}$, i.e., increasing coverage of the interface with pores. Note that these two relationships only provide an estimate for the upper and lower bound of R_{CT} and C_{CT}, respectively, because heterogeneous current distributions at the interface with respect to $A_{WE|SE}$ and $A_{WE|Pore|SE}$ will lead to deviations. In particular, in the limiting case where conduction across the pores is orders of magnitude better than across the physical contacts, no significant CT contribution is expected in the impedance spectrum since the dominant current paths do not cross physical contact spots. The observed deviations of the absolute values of the slopes of the linear fitting curves from a value of 1 in Figure 5b,c,g,h are due to the contributions of the interface areas with the much higher impedance, which are connected in parallel to the fraction of the interface carrying most of the transport, i.e., the pores in case of $\tau_{CT} < \tau_{Cstr}$ and the physical contacts in case of $\tau_{CT} < \tau_{Cstr}$. This has been recently discussed in more detail in the literature.[30]

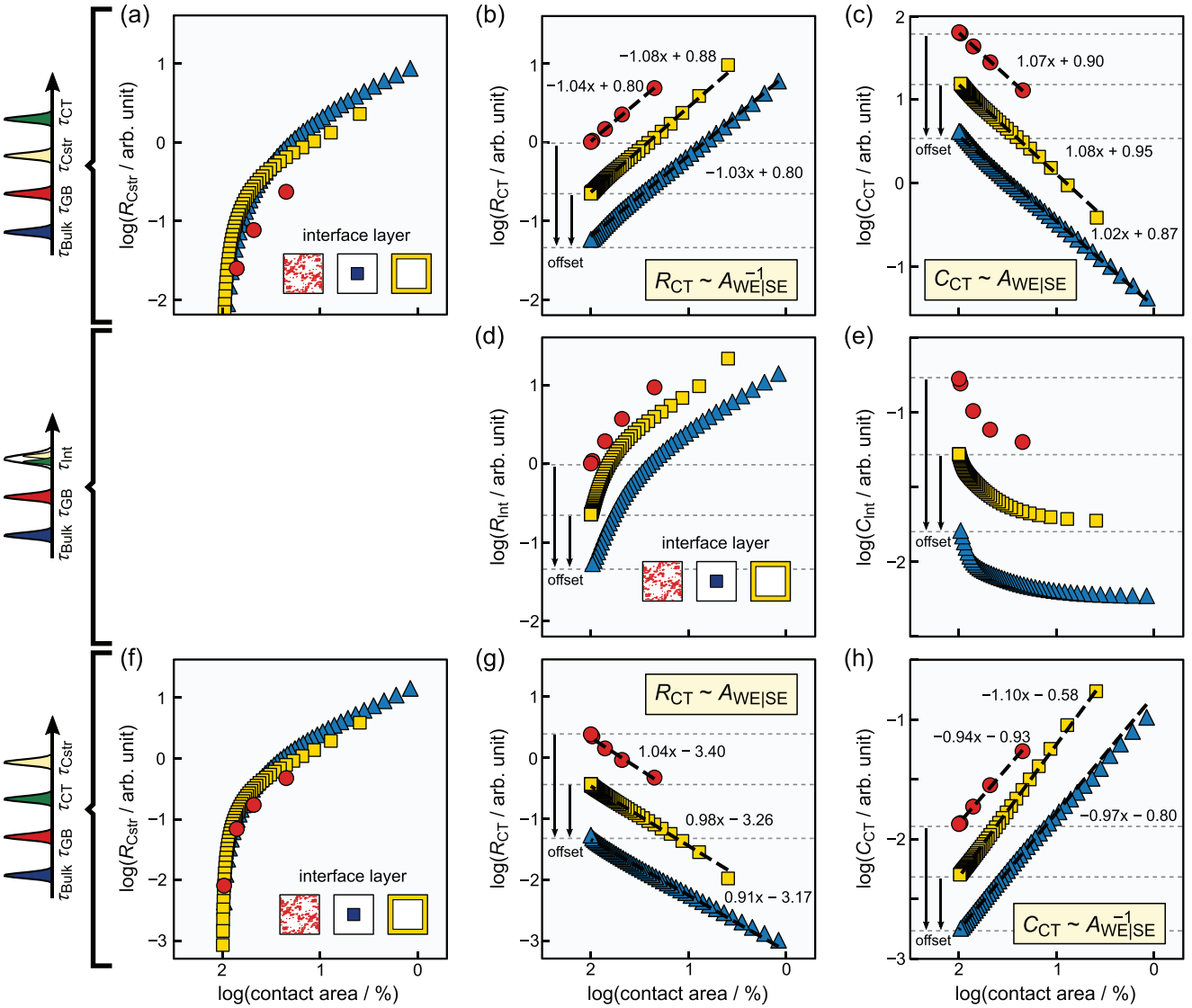

Figure 5. Functional dependence of interface contributions with the contact area $A_{WE|SE}$ considering different orders of time constants, i.e., a–c) $\tau_{Cstr} < \tau_{CT}$, d,e) $\tau_{Cstr} \approx \tau_{CT}$, and f–h) $\tau_{CT} < \tau_{Cstr}$. The dashed horizontal lines indicate an artificial offset along the *y*-axis for an improved comparability of the computational results. The non-linear behavior and strong dependence of R_{Cstr} on the interface morphology impedes the derivation of a universal functional relationship with the contact area. The CT resistance R_{CT} and capacitance C_{CT} are inversely proportional and proportional to the contact area, respectively, when $\tau_{Cstr} < \tau_{CT}$. The dependence of both parameters on the contact area is reversed in the case of $\tau_{CT} < \tau_{Cstr}$. The slight variations in the slop of the linear fits are due to the competing dielectric transport process through the pores at the interface.

The dependence of the effective interface parameters (R_{Int}, C_{Int}) on the physical contact area $A_{WE|SE}$ is shown in Figure 5d,e. These macroscopic transport quantities correspond to the situation in which only one interface impedance contribution can be observed, i.e., the intermediate case where $\tau_{Cstr} \approx \tau_{CT}$. As somewhat anticipated from the discussion above, no simple functional relationships are found between log R_{Int} versus log $A_{WE|SE}$ and log C_{Int} versus log $A_{WE|SE}$ because both, geometric constriction effect and CT contribute to one single signal. Starting from a minimum value at an ideal contact, the resistance log R_{Int} increases and the capacitance log C_{Int} decreases non-linearly with decreasing log $A_{WE|SE}$. The quantitative behavior observed depends on the interface morphology and the interplay of the materials parameters, as in the case of the pure constriction impedance. In particular, it is very sensitive to a variation of the polarization resistance describing the microscopic CT process.

So far, the following conclusions can be drawn from the discussion:

i) In the case of a porous interface, the geometric constriction effect disappears on the mesoscopic scale, when pressure is applied to the stack and the pores at the interface are closed due to plastic electrode deformation. In this limit and under the assumptions of chemical and thermodynamic stability of the interface, the interface impedance response is solely determined by the CT effect.

ii) The macroscopic constriction parameters (R_{Cstr}, C_{Cstr}) may differ even at the same $A_{WE|SE}$, if the morphology of the interface on the microscopic and mesoscopic scale varies, i.e., the spatial distribution of the physical contact area across the interface changes. The impact of geometric constriction is not negligible over a wide range of relative physical contact areas $A_{WE|SE}$, in particular for $A_{WE|SE} < 50\%$. Charge-transfer-driven morphological instabilities of interfaces always lead to an increase of the DC resistance independent of the microscopic polarization resistance underlying the CT process. As a result, geometric current constriction will have a major effect, for example, on the cycling behavior of battery cells.

iii) The functional relationship between the macroscopic transport parameters (R_i, C_i) of electric migration processes like CT and the relative physical contact area $A_{WE|SE}$ is not universal. It depends on the order of the time constants of individual interface impedance contributions. The correlation $R_{CT} \sim A_{WE|SE}^{-1}$ only holds for estimating the magnitude of the CT resistance R_{CT}, if the condition $\tau_{Cstr} < \tau_{CT}$ is fulfilled. In the case of $\tau_{CT} < \tau_{Cstr}$, the resistance R_{CT} depends linearly on the contact area $R_{CT} \sim A_{WE|SE}$. Similarly, for the CT capacitance, it holds $C_{CT} \sim A_{WE|SE}$ for $\tau_{Cstr} < \tau_{CT}$ and $C_{CT} \sim A_{WE|SE}^{-1}$ for $\tau_{CT} < \tau_{Cstr}$.

Temperature Dependence of Charge Transfer and Constriction Resistance: Battery cells are exposed to different environmental conditions in applications. Thus, studies of the influence of the environment on the cell performance are essential. The temperature-dependence is of particular interest, since internal (e.g., heating) and external (e.g., ambient) temperature variations occur during operation in most applications and will lead to changes of all impedance contributions. The previous discussion of the dependence of the macroscopic parameters (R_{Cstr}, C_{Cstr}) and (R_{CT}, C_{CT}) on stack pressure (i.e., physical contact area) has already underlined that their behavior is very different. The former can be considered as geometric fit parameters in macroscopic 1D equivalent circuit models, whereas the later represent an electric transport process on the microscopic level. This implies that the resistance R_{Cstr} is not solely based on a conductivity or microscopic polarization resistance, but parameterizes the dynamic constriction effect. It is determined by contributions of all microscopic transport processes taking place close to the interface, and, in a sense, leads to a reduced active SE volume involved in the transport through the sample. In consequence, the temperature-dependence of the geometric parameter R_{Cstr} is not obvious and needs to be investigated as all the microscopic electric transport processes that contribute to it may have a different temperature-dependence, i.e., different action energies $E_{a,i}$.

For this purpose, we focus on one specific morphology of the 3D model system for which the physical contact area is $A_{WE|SE} = 22\%$ and the interface has the realistic disordered morphology depicted in Figure 1c. The temperature-dependence of the ionic migration processes, i.e., of bulk and GB transport within the SE as well as of CT at the interface, are described by an Arrhenius behavior, for example, $\sigma(T) \sim \sigma_0/T \cdot \exp[-E_a / (k_B \cdot T)]$. The values assumed for the activation energies $E_{a,i}$ of the microscopic transport processes are given in the Computational Details section. The permittivity values are considered to not dependent on temperature. We computed series of impedance spectra at temperatures between –40°C and 40°C and derived the macroscopic transport parameters (R_i, C_i) of the individual processes at each temperature by fitting the resulting spectra with the 1D equivalent circuit model. Variations of microscopic conductivities σ_i with temperature T are directly reflected in the macroscopic resistance values R_i derived by the fitting approach. Thus, the individual activation energies $E_{a,i}$ can be determined from the slopes of corresponding Arrhenius diagrams $\ln[T/(R \cdot A)]$ versus T^{-1}, using the macroscopic resistance parameters R_i.

Similar to the former discussion, we consider again the three cases of different orders of the time constants τ_{Cstr} and τ_{CT}. Here, we will not discuss the activation energies $E_{a,i}$ of the macroscopic resistances R_i corresponding to the microscopic electric migration processes, i.e., the CT at the interface, bulk, and GB transport. Their activation energies almost agree with those of the corresponding microscopic input parameters, i.e., that of the polarization resistance R_{Pol} and those of the bulk and GB conductivities σ_i. Instead, we will solely analyze the effective activation energy of the macroscopic resistance parameters R_{Cstr} used for the parameterization of the constriction phenomenon in the 1D equivalent circuit model and R_{Int}, in the case of $\tau_{Cstr} \approx \tau_{CT}$, which is also strongly affected by current constriction.

Figure 6a shows Arrhenius diagrams of the constriction resistance R_{Cstr} in the case of $\tau_{Cstr} < \tau_{CT}$. Five different sets of microscopic transport parameters (σ_i, ε_i) were considered in the computations. Starting with a reversible WE|SE interface and highly conducting GBs ($Z_{CT} = Z_{GB} = 0$, blue data points), the activation energy $E_{a,Cstr}$ of the constriction resistance R_{Cstr} is 0.34 eV and identical to that of the microscopic bulk transport $E_{a,Bulk}$. This agrees with the observations of Fleig and Maier who exclusively considered a homogenous SE and no CT step at the interface in their early theoretical studies.[31–33] The activation energy $E_{a,Cstr}$ increases slightly to 0.35 eV, when the GBs become resistive ($Z_{GB} \neq 0$, $Z_{CT} = 0$, red data points). The effect is only marginal for the sample configuration and transport parameters considered, although the activation energy assigned to microscopic GB transport with 0.43 eV is rather high compared to the bulk value of 0.34 eV. This is due to the fact that the electric transport properties of the entire system are dominated by bulk transport ($R_{Bulk} \approx 12 \cdot R_{GB}$). The effect of the additional electric GB transport on R_{Cstr} would be more pronounced for decreasing conductivity σ_{GB} or a more prominent GB microstructure (i.e., an increased GB volume fraction and more GBs to be crossed along the dominant transport path). Interestingly, assuming a non-zero microscopic polarization resistance at the interface ($Z_{GB} \neq 0$, $Z_{CT} \neq 0$, greenish data points) does not alter $E_{a,Cstr}$ despite the high value of $E_{a,CT}$ with 0.43 eV, even when R_{Pol} is varied by an order of magnitude ($R_{Pol} \rightarrow 10 \cdot R_{Pol}$). The reason is that in the case of $\tau_{Cstr} < \tau_{CT}$, the transport processes across the interface, i.e., across both the pores and the physical contact area, are predominantly dielectric in the frequency range close to $1/\tau_{Cstr}$. In consequence, R_{Cstr} and $E_{a,Cstr}$ are not affected by the electric transport step across the physical contact $A_{WE|SE}$ and thus by the polarization resistance.[30]

In Figure 6b, we consider the case of comparable relaxation times $\tau_{Cstr} \approx \tau_{CT}$ and study the activation energy $E_{a,Int}$

ADVANCED MATERIALS INTERFACES
Open Access
www.advmatinterfaces.de

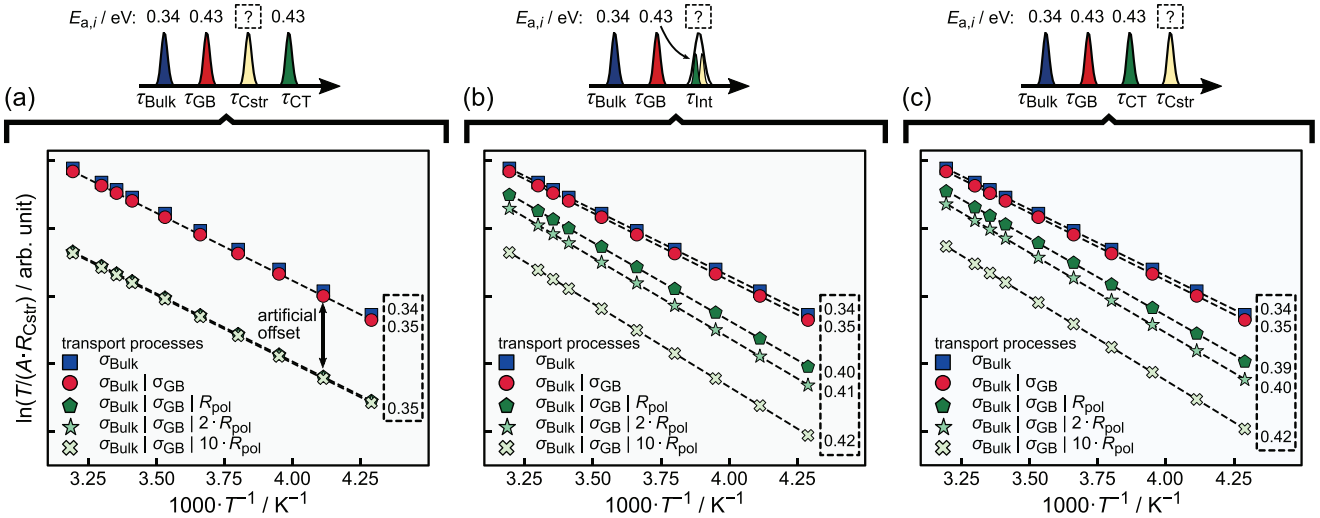

Figure 6. The constriction resistance R_{Cstr} is composed of contributions of all electric transport processes within the system. Its activation energy (numbers is dashed box) depends solely on the activation energy of the individual transport processes $E_{a,i}$. Only electric charge transport processes in the frequency range around $1/\tau_{Cstr}$ have an effect on the constriction resistance R_{Cstr}. Thus, a) the microscopic polarization resistance has no effect if $\tau_{CT} > \tau_{Cstr}$ and b,c) it affects $E_{a,Cstr}$ if $\tau_{CT} \leq \tau_{Cstr}$. The legend indicates the relative changes of the microscopic transport parameters in the computed impedance series. Note that the red and green points in (a) overlap and are only shifted along the *y*-axis for clarity.

of the single effective macroscopic interface resistance R_{Int}. In the frequency range of the interface impedance, pores are still almost dielectrically conductive while the transport across the physical contact takes place electrically. The transport situation resembles that for R_{Cstr} in the case of $\tau_{CT} < \tau_{Cstr}$, where the corresponding Arrhenius diagrams are displayed in Figure 6c. In both cases, the microscopic electric CT process at the interface is contributing to or even dominating the macroscopic resistances R_{Int} or R_{Cstr}, respectively. As a result of the frequency-dependent changes of the active SE volume for frequencies around $1/\tau_{Cstr}$, the averaging of the microscopic transport processes yielding R_{Int} and $E_{a,Int}$ or R_{Cstr} and $E_{a,Cstr}$ also changes.

The trends for the Arrhenius diagrams and the activation energies extracted are very similar, when looking at the five sets of microscopic transport parameters. The findings in the case of a reversible WE|SE interface considering highly conducting GBs ($Z_{CT} = Z_{GB} = 0$, blue data points) or resistive GBs ($Z_{GB} \neq 0$, $Z_{CT} = 0$, red data points) are similar to the results for $\tau_{Cstr} < \tau_{CT}$ shown in Figure 6a. The activation energy $E_{a,Int}$ or $E_{a,Cstr}$ equals that of the bulk process with 0.34 eV or increases only slightly to 0.35 eV due to the specific constellation and choice of materials parameters, respectively. Interestingly, the microscopic polarization resistance R_{Pol} now dominates the overall behavior of the macroscopic constriction resistance ($Z_{GB} \neq 0$, $Z_{CT} \neq 0$, greenish data points) for such an order of time constants. The activation energy $E_{a,Cstr}$ approaches that of the CT effect $E_{a,CT}$ with 0.43 eV, the more resistive the interface becomes, i.e., for increasing R_{Pol}. The activation energies of the effective interface resistance R_{Int} in Figure 6b tend to be slightly higher compared to those of pure constriction R_{Cstr} in Figure 6c. The reason is that R_{Int} includes a pure contribution of the macroscopic CT resistance R_{CT} based on the microscopic R_{Pol}, which typically has a higher activation energy than R_{Cstr} as originating from a microscopic migration process.

Altogether, the results on the temperature-dependence of R_{Cstr} and R_{Int} imply that the activation energies determined from Arrhenius diagrams reflect a weighting over all microscopic migration processes within the system. This indicates a relationship according to $R_{Cstr} = \Sigma_i\, \alpha_i \cdot 1/\sigma_i$ and a corresponding equation for R_{Int}. The weights α_i depend, for example, on the interface morphology, the contact area, the microstructure of the SE, the locations of GBs within the system and the order of the time constants of the individual transport processes. In particular, it holds that $\alpha_i \approx 0$, if $\tau_{Cstr} < \tau_i$.[30] The equation also implies that there is a range of values for $E_{a,Cstr}$ or $E_{a,Int}$ with boundaries given by the lowest and highest activation energies $E_{a,i}$ with $\alpha_i \neq 0$ of electric migration processes, i.e., $\min(E_{a,i}) \leq E_{a,Cstr} \leq \max(E_{a,i})$. This is due to the fact that $E_{a,Cstr}$ or $E_{a,Int}$ are a weighted average over the microscopic activation energies $E_{a,i}$ present in the system.

3.2.2. Effect of SEI Formation Due to Chemical Instabilities at Morphologically Stable Interfaces

Next, we turn to the right branch in the decision tree shown in Figure 2 and include the (electro)chemical instability of metal|SE interfaces. To our knowledge, there are only a few solid electrolytes that form an electrochemically and kinetically stable interface with alkali metals. Examples are the interfaces between lithium metal and garnets.[51–54] More common is the formation of an SEI (i.e., usually a multi-phase and nanoscale composite) at the interface, which usually exhibits less favorable charge transport properties, in particular a lower ionic conductivity than the SE itself. Here, the SEI is often continuously formed at the interface during operation, for example, when considering argyrodite-type SEs versus lithium metal.[10–14] The dynamic formation process corresponds to a transition from a WE|SE interface into a WE|SEI|SE layered interface over

time – ignoring the many inner homo- and hetero-interfaces in the SEI itself. In the following we will therefore consider the SEI as a homogeneous phase for the sake of simplicity and as there is not enough knowledge on the composition of the SEI. At the end of this process, the SEI layer covers the entire interface and is morphologically stable. In consequence, the impedance response of the interface is exclusively determined by the SEI. This situation corresponds to the first leaf node in the right branch in the decision tree in Figure 2. The increasing thickness δ_{Int} of the SEI will lead to an increase of its resistance ($R_{SEI} \sim \delta_{Int}$) and a decrease of its capacitance ($C_{SEI} \sim 1/\delta_{Int}$). The transport behavior across the interface is more complex, when the interface is only partially covered by the SEI layer. This may be due to the presence of pores at the interface or ideal metal-SE contact areas. In such cases, the effect on the impedance response of the system is not clear and needs to be studied in detail on the basis of microstructural information of the corresponding samples.

Corresponding experimental interface morphologies are, for example, described in a recent study by Otto et al., when bringing lithium foil with a passivation layer on its surface (e.g., Li_2CO_3, LiOH or Li_2O) into contact with a garnet-type SE.[57] The surface roughness of the SE leads to local penetrations of the passivation layer, which leads to a distribution of energetically preferred $A_{WE|SE}$ contacts and less preferred $A_{WE|SEI|SE}$ contacts at the interface. The interface structure described represents the third leaf node in the right branch of the decision tree in Figure 2. Apparently, the interface morphology seems to show many similarities to the porous interfaces considered in the previous section. Thus, we only substitute the pores by a resistive SEI (or passivation) at the interface within the theoretical 3D model system, i.e., we assume that the aging of the interface is exclusively caused by an SEI. The adapted interface morphology consists of a single contact spot $A_{WE|SE}$ in the middle of the electrode surrounded by an SEI layer $A_{WE|SEI|SE}$ (see inset in **Figure 7**a).

Again, we perform a series of impedance computations mimicking that the microstructure of the SE is kept constant and a gradual degradation of the WE|SE occurs, this time due to the formation of an SEI layer. The capacitance $\tilde{C}_{SEI}$ and resistance $\tilde{R}_{SEI}$ of the SEI are set to 100 Ω cm^2 and 88 µF cm^{-2}, respectively. Without loss of generality, the microscopic polarization resistance R_{Pol} at the two-phase boundary $A_{WE|SE}$ is assumed to be negligible ($Z_{CT} = 0$), i.e., there is no macroscopic CT signal in the impedance spectra. It represents a limiting case, experimentally observed for the interface between lithium metal and LLZO.[37,58–59] This assumption significantly simplifies the data analysis. Otherwise, the impedance response will depend on the interplay of interface time constants τ_{CT} and τ_{SEI} in a similar way discussed in the previous section for the simultaneous presence of CT and pores at the interface.

Figure 7a shows the modelled impedance data for five different contact areas in the range between 100% and 4.3% in Nyquist representation. The respective interface morphologies are displayed on the right with the two-phase boundary contact as a gray square in the center of the interface area and the light blue three-phase layered contact surrounding it such, that $A_{WE|SE} + A_{WE|SEI|SE} = 100\%$. The impedance spectrum for an ideal contact without SEI ($A_{WE|SE} = 100\%$) consists of two well-separated semicircles representing bulk (blue) and GB (red) transport within the SE. An additional interface semicircle (yellow) is formed in the spectra, when $A_{WE|SE}$ decreases, i.e., an SEI forms. At first glance, the qualitative impedance behavior seems to be similar to the case of a porous interface discussed in the previous section. Bulk and GB impedance remain unchanged, while the interface impedance increases with decreasing $A_{WE|SE}$ (cf. Figure 3a). To study the frequency-dependence of the resulting interface signal, we performed a DRT analysis of all impedance spectra as shown in Figure 7b. The relaxation times of the bulk and GB signals are again independent of the SEI fraction at the interface. Interestingly, the time constant of the interface signal τ_{Int} does not match the time constant of the microscopic electric transport process across the SEI layer τ_{SEI}. Instead, it exhibits a relaxation time in the intermediate range between GB and SEI time constant ($\tau_{GB} < \tau_{Int} < \tau_{SEI}$).

To study the functional behavior of the interface time constant τ_{Int} in more detail, we consider the dependence of the macroscopic transport parameters (R_{Int}, C_{Int}), derived by the 1D fitting approach of the computed impedance spectra, on the contact area $A_{WE|SE}$ (see Figure 7c,d). The macroscopic transport quantities of the 1D fitting model, i.e., bulk (green) and GB (orange) resistances as well as the SEI resistance and capacitance (cyan), are given as reference values in the figures. As expected, the resistance R_{Int} increases and the capacitance C_{Int} decreases with decreasing $A_{WE|SE}$, but the quantitative changes do not fit those of an electric migration process. Both parameters converge towards the limiting case of a completely covered interface ($R_{Int} \rightarrow R_{SEI}$, $C_{Int} \rightarrow C_{SEI}$ for $A_{WE|SE} \rightarrow 0$), instead of being (inversely) proportional to changes of the contact area. The same holds for the variation of the time constant ($\tau_{Int} \rightarrow \tau_{SEI}$ for $A_{WE|SE} \rightarrow 0$) as shown in Figure 7e. Consequently, the observed interface impedance signal does not represent the pure characteristics of the SEI or passivation as typically assumed in the literature. Instead, the macroscopic parameters (R_{Int}, C_{Int}) are also affected by the bulk and GB conductivity within the SE as well as the microscopic polarization resistance at the interface. These parameters influence the amounts of current flowing across the two-phase boundary described by $A_{WE|SE}$ and the layered three-phase contact described by $A_{WE|SEI|SE}$ at frequencies close to $1/\tau_{Int}$. The influence of the SEI properties on (R_{Int}, C_{Int}) increases as $A_{WE|SE}$ decreases, since the fraction of current flowing through the SEI layer increases.

The transport situation at the interface will change, if also pores are present at the interface in addition to a non-uniform SEI layer. When there is no direct contact between the metal and the SE (i.e., $A_{WE|SE} = 0\%$), the interface impedance behaves similarly to the studies performed in the previous chapter. Herein, the SEI contact $A_{WE|SEI|SE}$ takes the role of the ideal $A_{WE|SE}$ areas. The morphology corresponds to that of the second leaf node in the right branch of the decision tree in Figure 2. Note that in this situation, the effects of the microscopic transport parameters of the SEI layer ($\tilde{R}_{SEI}$, $\tilde{C}_{SEI}$) on the interface impedance are comparable to those of the CT reaction (R_{Pol}, C_{DL}) in the former case.[30] Impedance data evaluation becomes even more complex when there are also ideal $A_{WE|SE}$ areas at the interface (see fourth leaf node in the right branch of the decision tree in Figure 2). In this case, there is not only an interplay between the transport across

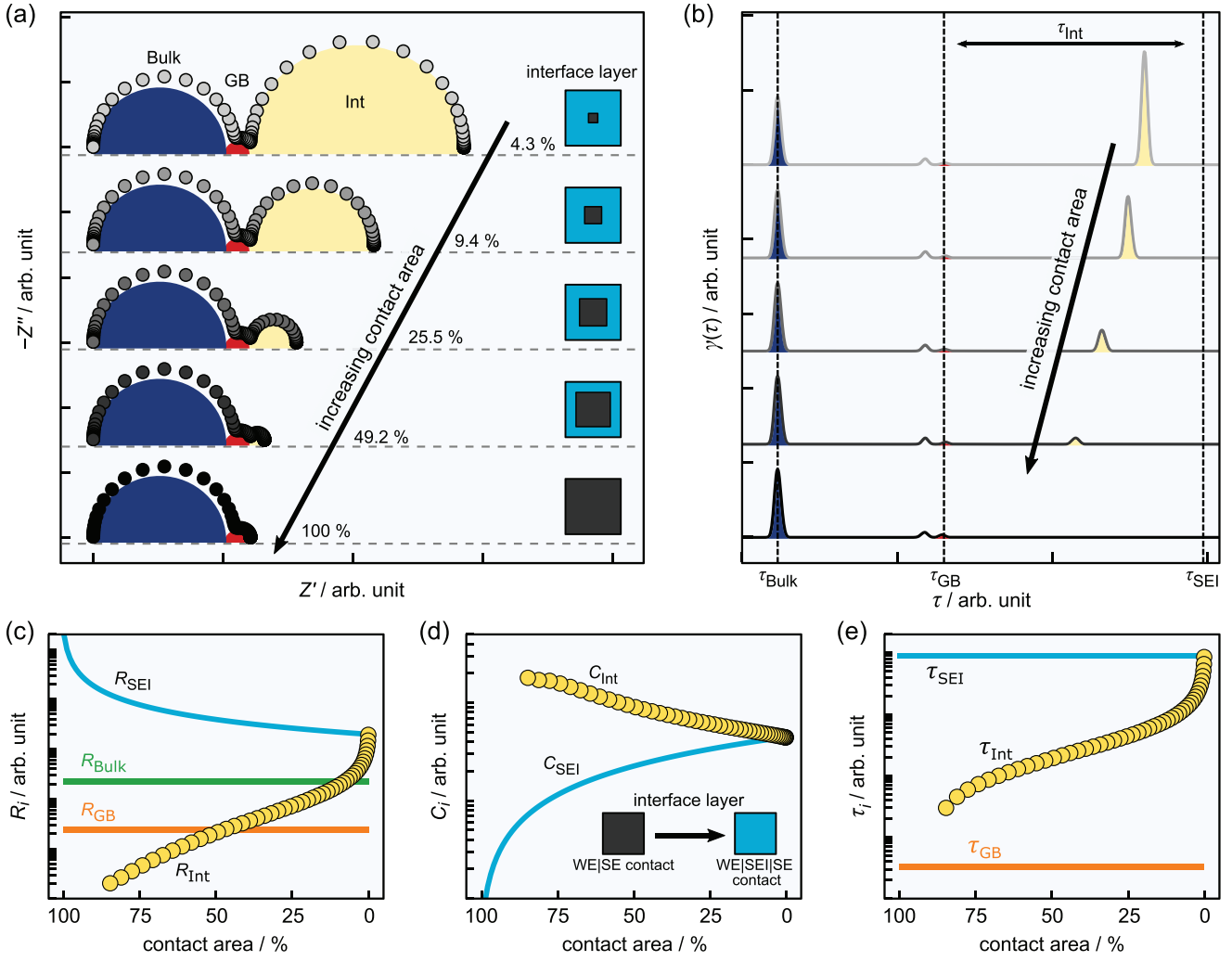

Figure 7. Impact of the successive evolution of an SEI layer (cyan) at the interface on the impedance response of the system. a) An additional interface contribution is formed in the impedance spectrum as the contact area $A_{WE|SE}$ decreases. Note that for simplicity, the CT step at $A_{WE|SE}$ was not considered in the modeling. b) The time constant of the interface signal does not match that of the microscopic transport through the SEI, if the interface is not fully covered. Evolution of the macroscopic transport parameters of the interface impedance, i.e., c) the resistance, d) the capacitance, and e) the time constant. Their qualitative behavior is similar to that of geometric constriction due to pore formation (cf. Figure 4). The macroscopic SEI (cyan), bulk (green), and GB (orange) parameters are given as reference values.

the $A_{WE|SE}$ and $A_{WE|SEI|SE}$ areas, but also across the $A_{WE|Pore|SE}$ contact. Basically, the active electrode area can then change with frequency between three levels: (1) the $A_{WE|SE}$ contact, (2) the $A_{WE|SE}$ + $A_{WE|SEI|SE}$ contact, and (3) the entire electrode area. Therefore, three impedance contributions are generally expected in such a situation. Apparently, the exact form of the interaction and the evolution of the interface contribution depends on the morphology of the interface, the individual microscopic transport quantities, and the order of the individual time constants.

In summary, the impedance signal for partially covered interfaces $A_{WE|SE} > 0\%$ at different relative contact areas and temperatures behaves similarly to that in the presence of geometric constriction for porous interfaces (cf. Figure 4). The main difference is the slightly different convergence behavior for $A_{WE|SE} \to 0$, i.e., $R_{Int} \to R_{SEI}$ and $C_{Int} \to C_{SEI}$ in the case of SEI formation instead of $R_{Cstr} \to \infty$ and $C_{Cstr} \to \tilde{C}_{Pore}$ in the case of pores. Distinguishing between constriction due to SEI or pores gets more difficult, when the SEI resistivity increases. This leads to a similar frequency-dependence of the systems and especially a similar interface impedance behavior. It should be noted that the interface impedance reflects the pure SEI characteristics only, when the interface is fully covered.

3.3. Strategies for the Identification of Interfacial Processes

The identification of the rate-limiting process at the interface is an essential starting point for improving the overall characteristics of a solid-state battery cell with a metal anode. Only in rare cases, a single process determines the electric properties of an all-solid metal|SE interface as shown in the decision tree in Figure 2. Typically, several effects contribute to the impedance response of

the interface. Examples from the microscopic to the mesoscopic level are the CT step at the two-phase boundary $A_{WE|SE}$, geometric constriction due to pores, or an SEI resulting in a layered three-phase contact $A_{WE|Pore|SE}$ or $A_{WE|SEI|SE}$. A macroscopic static constriction effect may occur, if the area at which the macroscopic WE is deposited on the SE surface is smaller than the latter, i.e., $A_{WE} < A_{SE}$.[29] However, this can be easily avoided by an appropriate contact preparation, for example, via sputter deposition. In what follows, we assume that the stacks are prepared such that all macroscopic layers have the same lateral dimensions.

The discussion in the previous sections has clearly shown that a careful analysis of the impedance data, in particular as a function of pressure, in the time or frequency domain allows the identification of the rate-limiting process at the interface in many cases. This holds especially for static situations, in which no SEI is dynamically formed or transformed during operation. It refers to systems with chemically stable interfaces and also to systems forming a kinetically stabilized interlayer (i.e., a uniform static secondary phase). Based on the derived criteria, we exemplarily define a strategy for experimentalists to follow in order to identify the origin of the interface impedance signals in recorded experimental spectra for symmetric Me|SE|Me arrangements, as described in Figure 1. In this situation, only CT and constriction effects determine the interface properties. The recipe for analyzing corresponding impedance data comprises several steps. The analysis is best performed in the time-domain according to the hierarchical scheme shown in **Figure 8**.

- Step 1: *Collection of impedance data at different stack pressures and performance of the corresponding DRT analyses.*

  Record an impedance spectrum of the pristine sample and perform a DRT analysis. The DRT will reveal either three or four main signals. The two signals at the shortest relaxation times τ usually correspond to transport processes within the SE, i.e., in the bulk of grains and across GBs. The remaining signals originate from the interface.

  i) If constriction and CT processes differ sufficiently in their characteristic time constants τ_i, two interface signals arise in the DRT (left branch).
  ii) If not, the signals due to the two interface processes overlap in the DRT (right branch).

- Step 2: *Behavior of the interface DRT signals under applied pressure.*

  Controlled application of stack pressure results in a continuous tuning of a porous interface morphology. Pores will gradually close with increasing pressure until an ideal and non-porous interface results at the highest pressures, i.e., $A_{WE|SE} \rightarrow 100\%$. This leads to a vanishing geometric constriction contribution. The DRT signal due to geometric constriction will exhibit a continuous change of the time constant (see black horizontal arrow in Figure 8) with the applied pressure and will vanish at the highest pressure at which the interface is ideal.

  i) In the case of two (separate) resolved interface signals, the one with decreasing amplitude and with changes in time constant as a function of pressure results from geometric current constriction. The time constant of the interface signal due to electric CT is independent of stack pressure, but its amplitude will also slightly change.
  ii) In the case of overlapping interface signals, the characteristic time constant of the single peak at the highest pressure will solely correspond to the CT effect. If no DRT signal can be resolved at the highest pressure, it is likely that dynamic constriction determines the overall interface properties of the system.

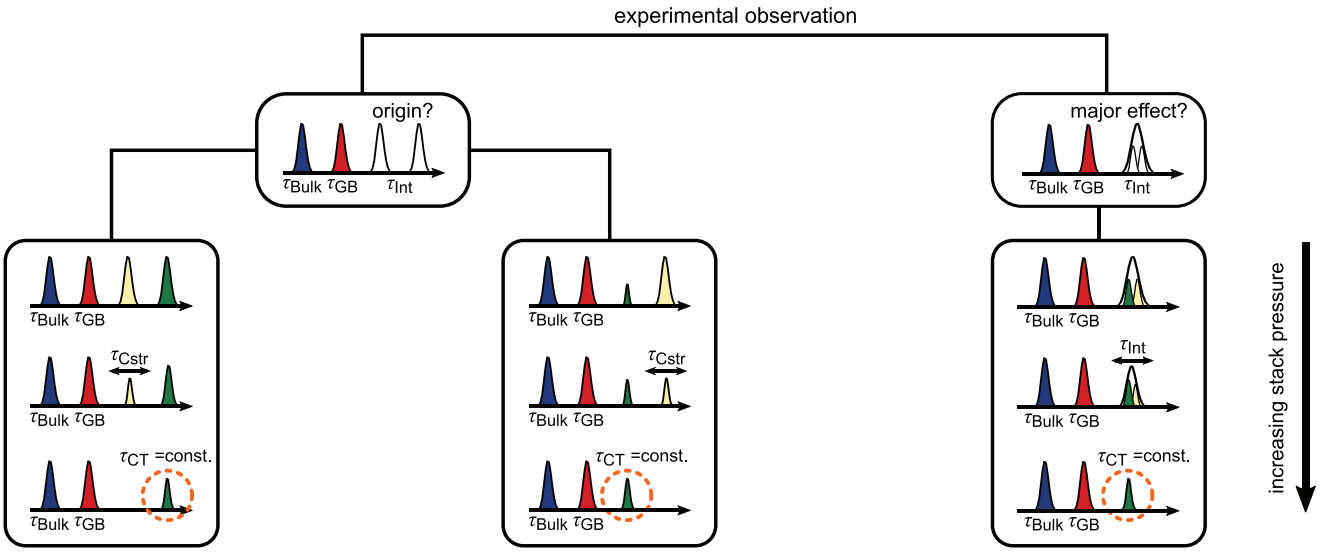

Figure 8. Guideline for assigning individual impedance signals to microscopic processes and estimating their magnitude on the systems interface properties in the case of chemically stable interfaces. The qualitative behavior for different stack pressures strongly depends on the order of time constants τ_i. In the limiting case of full physical contact $A_{WE|SE} = 100\%$, geometric current constriction signals vanish in the impedance spectrum.

- Step 3: *Determination of the macroscopic transport parameters of the CT effect.*

  The remaining interface signal at the highest pressure is solely due to the CT effect. This means that the 1D equivalent circuit model used for fitting this experimental impedance spectrum in the frequency domain can be restricted to three *RC*-elements representing the two microscopic transport processes in the SE and that of the CT process at the interface. The macroscopic transport parameters for the CT effect based on the 1D fitting approach are given by the microscopic polarization resistance $R_{Int}(A_{WE|SE} = 100\%) = R_{CT}(A_{WE|SE}) = R_{Pol}$ and the double-layer capacitance $C_{Int}(A_{WE|SE} = 100\%) = C_{CT}(A_{WE|SE}) = C_{DL}$.

- Step 4: *Determination of the macroscopic transport parameters.*

  i) If two interface contributions are observed, the series of impedance spectra taken at different pressures can be fitted by a 1D equivalent circuit model consisting of four *RC*-elements, i.e., (R_{Bulk}, C_{Bulk}), (R_{GB}, C_{GB}), (R_{CT}, C_{CT}), and (R_{Cstr}, C_{Cstr}). This holds for $A_{WE|SE} < 100\%$, i.e., apart from the highest pressures applied where the impedance response does not vary anymore. Only (R_{Cstr}, C_{Cstr}) and (R_{CT}, C_{CT}) should vary as a function of pressure, the parameters corresponding to the SE should be independent of pressure as the pores are typically dielectrically shorted in this frequency range. It should be noted that the electrode area may change during the application of stack pressure, requiring a specific normalization of the impedance spectra, as described in the literature.[37,49]

  ii) If only one interface contribution is observed, the series of impedance spectra taken at different pressures can be fitted by a 1D equivalent circuit model consisting of three *RC*-elements, i.e., (R_{Bulk}, C_{Bulk}), (R_{GB}, C_{GB}), and (R_{Int}, C_{Int}). Here, only (R_{Int}, C_{Int}) should vary as a function of pressure.

- Step 5: *Order of the time constants of the interface processes.*

  The dependence of R_{CT} and C_{CT} on pressure correlates with their dependence on the physical contact area $A_{WE|SE}$ as it increases with increasing pressure. Although $A_{WE|SE}$ is not necessarily a linear function of pressure, the observed dependence of $R_{CT}(p)$ and $C_{CT}(p)$ can be compared to the relations for $R_{CT}(A_{WE|SE})$ and $C_{CT}(A_{WE|SE})$ given in **Table 1**. This helps to identify the order of the characteristic time constants τ_{CT} and τ_{Cstr}, in the case that both signals do not overlap. The assignment should agree with the order of τ_i derived from the DRT series in step 2, and thus serves as a validation.

  i) R_{CT} increases with pressure and C_{CT} decreases with pressure, then $\tau_{CT} < \tau_{Cstr}$.
  ii) R_{CT} decreases with pressure and C_{CT} increases with pressure, then $\tau_{CT} > \tau_{Cstr}$.

  In the case of overlapping interface signals, the relations for $R_{CT}(A_{WE|SE})$ and $C_{CT}(A_{WE|SE})$, together with R_{Pol} and C_{DL} derived in step 3, help to estimate the magnitude of the CT effect for different pressures or contact areas and thus to identify the dominant interface effect.

- Step 6: *Correlation with structural properties.*

  The dependence of $R_{CT}(p)$ and $C_{CT}(p)$ can be translated, based on the theoretical dependence of $R_{CT}(A_{WE|SE})$ and $C_{CT}(A_{WE|SE})$ given in Table 1, into a functional relationship $A_{WE|SE}(p)$. This can be correlated with the results of the structural analysis of the pore distribution (e.g., via FIB SEM) in

Table 1. Overview of the characteristics of transport signals compared to signals of geometric origin.

$\tau_{Bulk} < \tau_{GB} < \tau_{Cstr} < \tau_{CT}$		$\tau_{Bulk} < \tau_{GB} < \tau_{CT} < \tau_{Cstr}$	
constriction	charge transfer	constriction	charge transfer
$\tau_{Cstr}(A_{WE\|SE}) \neq$ const.	$\tau_{CT}(A_{WE\|SE}) =$ const.	$\tau_{Cstr}(A_{WE\|SE}) \neq$ const.	$\tau_{CT}(A_{WE\|SE}) =$ const.
$R_{Cstr}(A_{WE\|SE})$: non-linear	$R_{CT} \sim 1/A_{WE\|SE}$	$R_{Cstr}(A_{WE\|SE})$: non-linear	$R_{CT} \sim A_{WE\|SE}$
$R_{Cstr}(A_{WE\|SE} \to 100\,\%) \to 0$	$R_{CT}(A_{WE\|SE} \to 100\,\%) \to R_{Pol}$	$R_{Cstr}(A_{WE\|SE} \to 100\,\%) \to 0$	$R_{CT}(A_{WE\|SE} \to 100\,\%) \to R_{Pol}$
$R_{Cstr}(A_{WE\|SE} \to 0\,\%) \to \begin{cases} \infty \\ \tilde{R}_{SEI} \end{cases}$	$R_{CT}(A_{WE\|SE} \to 0\,\%) \to \infty$	$R_{Cstr}(A_{WE\|SE} \to 0\,\%) \to \begin{cases} \infty \\ \tilde{R}_{SEI} \end{cases}$	$R_{CT}(A_{WE\|SE} \to 0\,\%) \to 0$
$C_{Cstr}(A_{WE\|SE})$: non-linear	$C_{CT} \sim A_{WE\|SE}$	$C_{Cstr}(A_{WE\|SE})$: non-linear	$C_{CT} \sim 1/A_{WE\|SE}$
$C_{Cstr}(A_{WE\|SE} \to 100\,\%) \to \infty$	$C_{CT}(A_{WE\|SE} \to 100\,\%) \to C_{DL}$	$C_{Cstr}(A_{WE\|SE} \to 100\%) \to \begin{cases} \infty, R_{pol} \downarrow \\ 0, R_{pol} \uparrow \end{cases}$	$C_{CT}(A_{WE\|SE} \to 100\,\%) \to C_{DL}$
$C_{Cstr}(A_{WE\|SE} \to 0\,\%) \to \begin{cases} \tilde{C}_{Pore} \\ \tilde{C}_{SEI} \end{cases}$	$C_{CT}(A_{WE\|SE} \to 0\,\%) \to 0$	$C_{Cstr}(A_{WE\|SE} \to 0\,\%) \to \begin{cases} \tilde{C}_{Pore} \\ \tilde{C}_{SEI} \end{cases}$	$C_{CT}(A_{WE\|SE} \to 0\,\%) \to \infty$
$E_{a,Bulk} < E_{a,Cstr} \leq E_{a,GB}$	$E_{a,Bulk} < E_{a,GB} \leq E_{a,CT}$	$E_{a,Bulk} < E_{a,Cstr} \leq E_{a,CT}$	$E_{a,Bulk} < E_{a,GB} \leq E_{a,CT}$
$E_{a,Cstr}(A_{WE\|SE}) \neq$ const.	$E_{a,i}(A_{WE\|SE}) =$ const.	$E_{a,Cstr}(A_{WE\|SE}) \neq$ const.	$E_{a,i}(A_{WE\|SE}) =$ const.

nominally equivalent samples treated at different pressures. Such comparisons serve as an additional validation of this data analysis approach.

- Step 7: *Correlation with temperature-dependent impedance measurements.*

Temperature-dependent measurements allow to extract thermal activation energies for the observed macroscopic resistances R_i deduced by the 1D equivalent circuit fitting approach with four or three *RC*-elements connected in series. Typically, the activation energy of the metal ion migration in the bulk electrolyte is less than that of ion transport across a grain boundary in the SE and this in turn is less than or equal to that of charge transfer at the metal|SE interface ($E_{a,Bulk} < E_{a,GB} \leq E_{a,CT}$). This consideration is based on the assumption that charge transfer $Me = Me^+ + e'$ is the rate-limiting kinetic step in the system rather than ion migration in the electrolyte phase. In consequence, the activation energy of the 1D fit parameter R_{Cstr}, which represents an average of all microscopic electric transport processes in the system, lies somewhere between that of the bulk and that of the CT process, i.e., $\min(E_{a,i}) \leq E_{a,Cstr} \leq \max(E_{a,i})$. However, the value depends not only on the magnitude of the individual microscopic activation energies $E_{a,i}$ (i = Bulk, GB, CT), which are independent of geometry, but also on the global character of the constriction effect, which defines the macroscopic sample volume contributing to the transport and thus the weights in the averaging of the microscopic activation energies.

Table 1 summarizes the functional behavior of the macroscopic transport parameters describing CT and constriction effect when fitting with 1D equivalent circuit models in the case of different situations characterized by the order of the time constants τ_{CT} and τ_{Cstr}. The clear dependences should be helpful in the interpretation of experimental impedance spectra. However, a word of caution is essential here. The dependences derived, of course, are to some extent affected by the assumptions about the 3D sample morphology (see Figure 1). Minor deviations are anticipated, for example, if not only the contact area $A_{WE|SE}$ but also the thickness δ_{Int} of the electrically insulating layer at the interface is varied. In particular, this has a major superimposed effect on the macroscopic constriction capacitance as $C_{Cstr} \sim \varepsilon_{Int}/\delta_{Int}$, in contrast to the constriction resistance as $R_{Cstr} = \Sigma_i\, \alpha_i \cdot 1/\sigma_i + \Sigma_j\, \alpha_j \cdot R_{Pol,\,j}$.

Establishing similar hierarchical schemes for analyzing the interface impedance response in cases, in which an SEI layer is dynamically formed, is in principle also possible. However, this will require additional structural information and probably will depend significantly on the materials involved. For example, in the cases in which a non-uniform secondary phase takes the place of pores at the interface, the assumption that the interface morphology approaches a state under pressure where $A_{WE|SE}$ = 100% is not valid. In consequence, the constriction effect will not disappear at high pressures, and thus the derived hierarchical scheme is not applicable. Therefore, it is essential to know how the two phases at the interface behave under pressure in order to establish a corresponding scheme for such cases. The situation in the case of dynamic SEI formation is

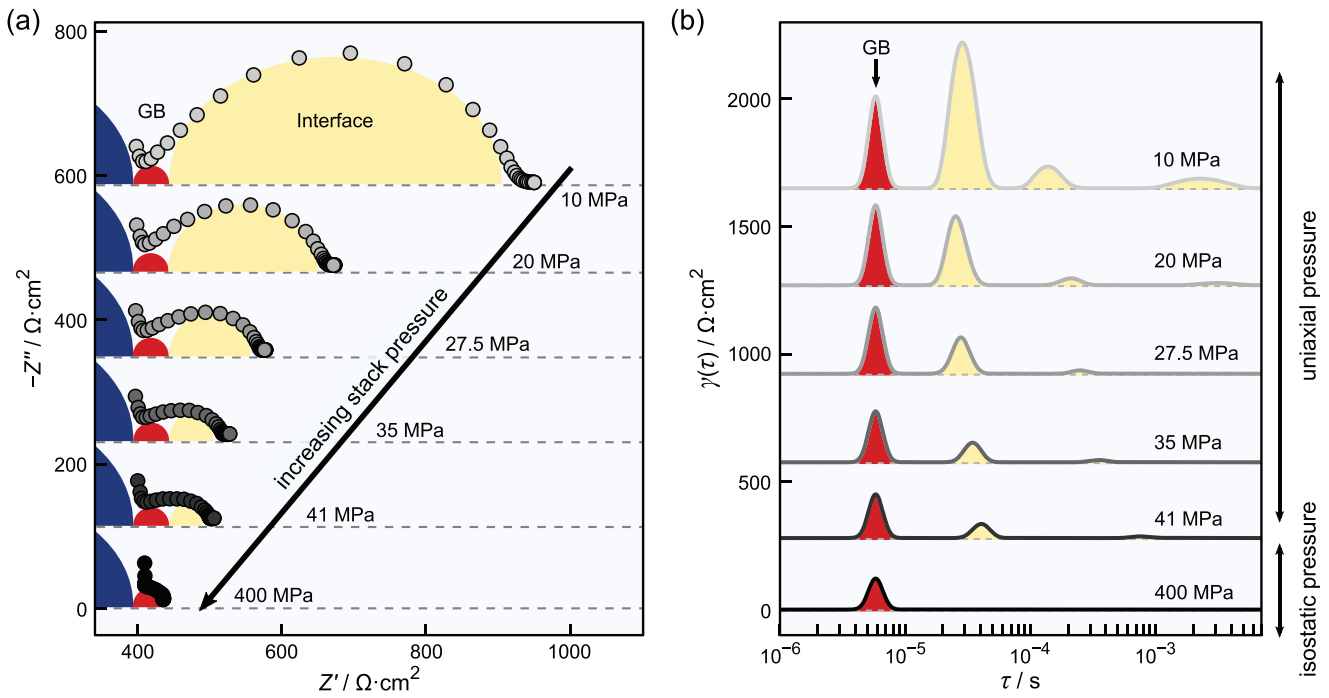

Figure 9. Experimental impedance data on the pressure-dependence of the interface impedance of a symmetric Li|LLZO|Li cell. The raw data originates from a recent study of Krauskopf et al. published in the literature. Adapted with permission.[37] Copyright 2019, American Chemical Society. The dashed lines indicate an artificial offset along the *y*-axis for visualization. a) The interface impedance (yellow) decreases with uniaxial pressure and vanishes after applying an isostatic pressure of 400 MPa. b) Even in the DRT analysis, there is no evidence for an interface signal at 400 MPa. Note that the bulk DRT signal could not be observed, since its impedance behavior is not fully captured in the measured frequency range.

even more complex as the SEI changes continuously during operation. If its temporal evolution is known from a structural analysis, the corresponding variation of the impedance spectra during operation may be addressed and meaningful parameters may be extracted. For example, if a closed SEI layer at the interface is formed, its macroscopic transport parameters R_{SEI} and C_{SEI} will vary systematically with its thickness δ_{Int}, according to $R_{SEI} \sim \delta_{Int}$ and $C_{SEI} \sim 1/\delta_{Int}$. The analysis may be quite intricate, once the SEI itself is porous, which is a natural consequence of a negative reaction volume of SEI formation.[14,45]

3.4. Evaluating the Effect of Individual Interface Processes between Lithium and LLZO

Finally, we present an experimental case study to demonstrate the applicability of the hierarchical scheme discussed in the context of Figure 8. The data, which are analyzed here in more detail, are those of Krauskopf et al. They comprise an investigation of the effect of stack pressure on the impedance response of a symmetric Li|LLZO|Li cell arrangement.[37] Resistive SEI formation can be ruled out for this material combination, since the garnet-type solid electrolyte LLZO is one of the few Li-ion conductors that is kinetically stable against lithium.[51–54] Furthermore, Krauskopf et al. performed a microstructural analysis of the interface region and identified pores for stack pressures smaller than 400 MPa.[60–64] Both pieces of information demonstrate that the experimental results fulfill the assumption underlying the hierarchical scheme previously presented.

Figure 9a shows a series of impedance spectra in Nyquist representation taken at various external pressures. The initial spectrum at 10 MPa uniaxial stack pressure consists of three separated semicircles, i.e., two from bulk (blue, ≈1 MHz) and GB (red, ≈10 kHz) transport in the SE, and one from transport across the interface (yellow, <1 kHz). The continuous increase of uniaxial pressure resulted in a decrease of the single interface signal, i.e., an initial resistance R_{Int} of about 300 Ω cm^2 at 10 MPa decreased to 50 Ω cm^2 at 41 MPa. Furthermore, the semicircles of bulk and GB transport remained unchanged, i.e., they are not influenced by the applied pressure. In the frequency domain, it seems that only one interface contribution is present as only one impedance signal can be discerned. Interestingly, no interface signal could be resolved anymore (<0.1 Ω cm^2) after further increasing the external load to an isostatic pressure of 400 MPa, i.e., only the unchanged bulk and GB semicircles were observed.

We proceed now stepwise according to our hierarchical scheme:

As step 1, we perform a DRT analysis of the impedance data. The resulting series of DRT at various pressures is shown in Figure 9b. Frequency points below 200 Hz were excluded in the analysis, since individual residuals were greater than 4% in the Kramers–Kronig test. Similarly, frequency points above 0.2 MHz were neglected as most of the bulk contribution (blue) is not captured in the measured frequency range. As a result, parts of the GB impedance (red) were not reflected in the considered frequency range, which affects the magnitude of the corresponding DRT signal. Thus, the analysis conducted can only reveal qualitative trends in the data. Nevertheless, the DRT of the initial impedance at 10 MPa consists of four signals. The one at low relaxation times represents transport across GBs (red), while the three broad signals at higher relaxation times result from the WE|SE interface (yellow) as the CE was prepared as ideal QRE. The occurrence of more than two interface signals in the experimental data is due to competing transport paths through the sample.[23]

As step 2, we identify the interface DRT signals whose characteristic time constant depends on pressure and assign its origin to the constriction effect. The time constant of the GB signal around 10^{-5} s is independent of stack pressure as expected. The three other DRT signals from interface possesses with relaxation times between 10^{-5} s and 10^{-2} s, all strongly depend on external load. Their time constants shift and their amplitudes decrease and vanish with increasing uniaxial pressure. No contribution from the interface can be observed after an isostatic pressure of 400 MPa was applied. This suggests that all three signals arise from the constriction effect and the CT effect is negligible in case of the Li|LLZO interface.

Several other aspects support the conclusion that current constriction rather than CT is the rate-determining step at the Li|LLZO interface. First, the estimate of the upper limit of the macroscopic CT resistance at small contact areas according to step 5, which yields about 1 Ω cm^2, several orders of magnitude lower than the experimentally observed values for R_{Int}.[59] Second, the structural analysis (corresponding to step 6 of the hierarchical scheme) reveals pores at the interface. This is even more supported by a theoretical study of Zhang et al. who suggest that the physical contact $A_{WE|SE}$ roughly changes by a factor of five in the experiment of Krauskopf et al., from around 20% at 10 MPa to almost 100% at 400 MPa.[39] Third, temperature-dependent impedance measurements (corresponding to step 7 of the hierarchical scheme) yield a small activation energy for the interface signal $E_{a,Int}$ = 0.37 eV comparable to that of the bulk process $E_{a,Bulk}$ = 0.34 eV.

All listed observations agree very well with the computations performed and also with fundamental studies on the constriction effect published in the literature.[29–36] Thus, we conclude that the CT step at the Li|LLZO interface is negligible as current constriction effects clearly dominate the electric Li|LLZO interface properties in the samples studied by Krauskopf et al. This result is consistent with several other experimental observations, such as the evolution and the increase of an interfacial (i.e., constriction) impedance contribution due to pore formation during anodic dissolution.[50,63,65–68] Moreover, Ortmann et al. recently reported similar experimental findings for the interface between sodium and NASICON-type solid electrolyte $Na_{3.4}Zr_2Si_{2.4}P_{0.6}O_{12}$.[49] Their detailed analysis of the origin of the interface impedance reveals that the contribution of a naturally grown and kinetically stabilized interphase is negligible. Instead, pore formation leads to current constriction, which dominates the rate performance at the interface. This further emphasizes the important role of geometric constriction effects at alkali metal|SE interfaces on the way towards the successful implementation of reversible metal anodes in the market.

4. Conclusions

Various processes, such as charge transfer, morphological and chemical instabilities due to pores or SEI formation, affect the interface properties of metal anodes in solid-state battery cells. Identifying the dominant interface effect(s) at metal|solid electrolyte interfaces is crucial, as the strategy for improving a solid-state battery depends on the rate-limiting process, which needs to be overcome. In this study, we use a 3D electric network model to investigate the interplay of these interface effects with the structural properties of a symmetric Me|SE|Me stack in order to assess their impact on the impedance data in the frequency and time domain.

We perform a thorough analysis of the dependence of the impedance data on the physical contact area $A_{WE|SE}$ and on temperature for different orders of the time constants of the underlying interface processes. Fitting the computed impedance data with 1D equivalent circuit models, in which different processes are represented by *RC*-elements, allows to translate the microscopic and mesoscopic transport properties into macroscopic transport parameters (R_i, C_i). This enables the development of universal recipes in the form of hierarchical schemes for analyzing experimental impedance data. We introduce such a scheme for systems with chemically stable interfaces, or with kinetically stabilized interlayer, for example, battery stacks with a porous WE|SE interface. The approach relies on the evolution of the impedance data when the porous interface morphology is continuously tuned under external pressure.

In principle, similar schemes can be developed for systems with other interface morphologies, e.g., interfaces with dynamic SEI formation. However, the impedance studies in such cases need to be accompanied by thorough structural investigations of the evolution of the interface morphology under operation or under external parameters like pressure. This is a necessity for extracting the functional relationship between the macroscopic transport parameters of the 1D equivalent circuit models and external control parameters tuned in the experiment. The approach sketched spans the bridge between 3D electric network modelling of impedance data and experimental measurements and corresponding analysis. It is widely employable and will help to speed up the optimization of solid-state batteries in the future.

This is successfully demonstrated considering experimental impedance data of a Li|LLZO|Li stack. We prove unambiguously that the Li|LLZO interface properties are dominated by geometric current constriction while the electric CT migration process plays only a negligible role. This also applies to recent experimental results on sodium in contact with a NASICON-type solid electrolyte. Consequently, charge-transfer driven morphological instabilities during cycling impedes the successful implementation of reversible metal anodes in the market. Thus, methods need to be developed to suppress pore formation at the WE|SE interface.

Acknowledgements

The authors greatly appreciate helpful discussions with Till Ortmann and Sascha Kremer. The authors thank Elisa Monte for the preparation of the graphical abstract. The authors acknowledge computational resources provided by the HPC Core Facility and the HRZ of the Justus-Liebig-University Giessen. The authors would like to thank MSc. Philipp Risius and Dr. Marcel Giar of HPC-Hessen, funded by the State Ministry of Higher Education, Research, and the Arts (HMWK), for programming advice. Financial support is provided by the DFG via the GRK (Research Training Group) 2204 "Substitute Materials for sustainable Energy Technologies". J.J. and S.B. acknowledge financial support by the German Federal Ministry of Education and Research within the cluster of competence FESTBATT (projects 03XP0177A and 03XP0180). J.J. and T.F. acknowledge funding by the German Federal Ministry of Education and Research (BMBF) of the LiSI and LiSI2 project, grant identifiers 03XP0224E and 03XP0509B. [Correction added on 22 August 2023, after first online publication: Projekt Deal funding statement has been added.]

Open access funding enabled and organized by Projekt DEAL.

Conflict of Interest

The authors declare no conflict of interest.

Data Availability Statement

The data that support the findings of this study are available from the corresponding author upon reasonable request.

Keywords

current constriction, interface impedance, lithium metal anodes, pore and SEI formation, solid-state batteries

Received: November 13, 2022
Revised: December 18, 2022
Published online: February 5, 2023

[1] C. Niu, H. Lee, S. Chen, Q. Li, J. Du, W. Xu, J.-G. Zhang, M. S. Whittingham, J. Xiao, J. Liu, *Nat. Energy* **2019**, *4*, 551.
[2] H. Wang, D. Yu, C. Kuang, L. Cheng, W. Li, X. Feng, Z. Zhang, X. Zhang, Y. Zhang, *Chem* **2019**, *5*, 313.
[3] M. T. McDowell, F. J. Q. Cortes, A. C. Thenuwara, J. A. Lewis, *Chem. Mater.* **2020**, *32*, 8755.
[4] Y. Takeda, O. Yamamoto, N. Imanishi, *Electrochemistry* **2016**, *84*, 210.
[5] J. M. Tarascon, M. Armand, in *Materials for Sustainable Energy*, Macmillan Publishers Ltd, London **2010**, pp. 171–179.
[6] K. Xu, *Chem. Rev.* **2004**, *104*, 4303.
[7] K. Nishikawa, T. Mori, T. Nishida, Y. Fukunaka, M. Rosso, T. Homma, *J. Electrochem. Soc.* **2010**, *157*, A1212.
[8] H. E. Park, C. H. Hong, W. Y. Yoon, *J. Power Sources* **2008**, *178*, 765.
[9] M. Weiss, F. J. Simon, M. R. Busche, T. Nakamura, D. Schröder, F. H. Richter, J. Janek, *Electrochem. Energy Rev.* **2020**, *3*, 221.
[10] J. Kasemchainan, S. Zekoll, S. D. Jolly, Z. Ning, G. O. Hartley, J. Marrow, P. G. Bruce, *Nature Mater.* **2019**, *18*, 1105.
[11] M.-C. Bay, M. Wang, R. Grissa, M. V. F. Heinz, J. Sakamoto, C. Battaglia, *Adv. Energy Mater.* **2020**, *10*, 1902899.
[12] R. Schlenker, D. Stępień, P. Koch, T. Hupfer, S. Indris, B. Roling, V. Miß, A. Fuchs, M. Wilhelmi, H. Ehrenberg, *ACS Appl. Mater. Interfaces* **2020**, *12*, 20012.
[13] S. D. Jolly, Z. Ning, G. O. Hartley, B. Liu, D. L. R. Melvin, P. Adamson, J. Marrow, P. G. Bruce, *ACS Appl. Mater. Interfaces* **2021**, *13*, 22708.
[14] L. M. Riegger, S.-K. Otto, M. Sadowski, S. Jovanovic, O. Kötz, S. Harm, L. G. Balzat, S. Merz, S. Burkhardt, F. H. Richter, J. Sann,

R.-A. Eichel, B. V. Lotsch, J. Granwehr, K. Albe, J. Janek, *Chem. Mater.* **2022**, *34*, 3659.
[15] V. Lacivita, Y. Wang, S.-H. Bo, G. Ceder, *J. Mater. Chem. A* **2019**, *7*, 8144.
[16] S. Wenzel, S. Randau, T. Leichtweiß, D. A. Weber, J. Sann, W. G. Zeier, J. Janek, *Chem. Mater.* **2016**, *28*, 2400.
[17] J. Janek, S. Majoni, *Ber. Bunsenges. Phys. Chem.* **1995**, *99*, 14.
[18] S. Majoni, J. Janek, *Ber. Bunsenges. Phys. Chem.* **1998**, *102*, 756.
[19] H. Schmalzried, J. Janek, *Ber. Bunsenges. Phys. Chem.* **1998**, *102*, 127.
[20] N. M. Beekmans, L. Heyne, *Electrochim. Acta* **1976**, *21*, 303.
[21] T. van Dijk, A. J. Burggraaf, *Phys. Status Solidi* **1981**, *63*, 229.
[22] M. J. Verkerk, B. J. Middelhuis, A. J. Burggraaf, *Solid State Ionics* **1982**, *6*, 159.
[23] J. K. Eckhardt, S. Burkhardt, J. Zahnow, M. T. Elm, J. Janek, P. J. Klar, C. Heiliger, *J. Electrochem. Soc.* **2021**, *168*, 090516.
[24] T. R. Jow, C. C. Liang, *J. Electrochem. Soc.* **1983**, *130*, 737.
[25] A. Schröder, J. Fleig, D. Gryaznov, J. Maier, W. Sitte, *J. Phys. Chem. B* **2006**, *110*, 12274.
[26] T. Krauskopf, B. Mogwitz, H. Hartmann, D. K. Singh, W. G. Zeier, J. Janek, *Adv. Energy Mater.* **2020**, *10*, 2000945.
[27] B. S. Vishnugopi, E. Kazyak, J. A. Lewis, J. Nanda, M. T. McDowell, N. P. Dasgupta, P. P. Mukherjee, *ACS Energy Lett.* **2021**, *6*, 3734.
[28] J. A. Lewis, F. J. Q. Cortes, Y. Liu, J. C. Miers, A. Verma, B. S. Vishnugopi, J. Tippens, D. Prakash, T. S. Marchese, S. Y. Han, C. Lee, P. P. Shetty, H. W. Lee, P. Shevchenko, F. De Carlo, C. Saldana, P. P. Mukherjee, M. T. McDowell, *Nat. Mater.* **2021**, *20*, 503.
[29] J. K. Eckhardt, P. J. Klar, J. Janek, C. Heiliger, *ACS Appl. Mater. Interfaces* **2022**, *14*, 35545.
[30] J. K. Eckhardt, T. Fuchs, S. Burkhardt, P. J. Klar, J. Janek, C. Heiliger, *ACS Appl. Mater. Interfaces* **2022**, *14*, 42757.
[31] J. Fleig, J. Maier, *Electrochim. Acta* **1996**, *41*, 1003.
[32] J. Fleig, J. Maier, *Solid State Ionics* **1996**, *86–88*, 1351.
[33] J. Fleig, J. Maier, *J. Electroceram.* **1997**, *1*, 73.
[34] J. Fleig, J. Maier, *Solid State Ionics* **1997**, *94*, 199.
[35] J. Fleig, J. Maier, *J. Electrochem. Soc.* **1997**, *144*, L302.
[36] J. Fleig, J. Maier, *J. Am. Ceram. Soc.* **1999**, *82*, 3485.
[37] T. Krauskopf, H. Hartmann, W. G. Zeier, J. Janek, *ACS Appl. Mater. Interfaces* **2019**, *11*, 14463.
[38] W. E. Tenhaeff, E. Rangasamy, Y. Wang, A. P. Sokolov, J. Wolfenstine, J. Sakamoto, N. J. Dudney, *ChemElectroChem* **2014**, *1*, 375.
[39] X. Zhang, Q. J. Wang, K. L. Harrison, S. A. Roberts, S. J. Harris, *Cell Rep. Phys. Sci.* **2020**, *1*, 100012.
[40] D. Rettenwander, A. Welzl, L. Cheng, J. Fleig, M. Musso, E. Suard, M. M. Doeff, G. J. Redhammer, G. Amthauer, *Lnorg. Chem.* **2015**, *54*, 10440.
[41] C. Loho, R. Djenadic, M. Bruns, O. Clemens, H. Hahn, *J. Electrochem. Soc.* **2016**, *164*, A6131.
[42] B. Boukamp, *Solid State Ionics* **2004**, *169*, 65.
[43] T. H. Wan, M. Saccoccio, C. Chen, F. Ciucci, *Electrochim. Acta* **2015**, *184*, 483.
[44] J. T. S. Irvine, D. C. Sinclair, A. R. West, *Adv. Mater.* **1990**, *2*, 132.
[45] S.-K. Otto, L. M. Riegger, T. Fuchs, S. Kayser, P. Schweitzer, S. Burkhardt, A. Henss, J. Janek, *Adv. Mater. Interfaces* **2022**, *9*, 2102387.
[46] A. Banerjee, X. Wang, C. Fang, E. A. Wu, Y. S. Meng, *Chem. Rev.* **2020**, *120*, 6878.
[47] K.-Y. Yang, C. Leu, K.-Z. Fung, M.-H. Hon, M.-C. Hsu, Y.-J. Hsiao, M.-C. Wang, *J. Mater. Res.* **2008**, *23*, 1813.
[48] X. Shen, Y. Li, T. Qian, J. Liu, J. Zhou, C. Yan, J. B. Goodenough, *Nat. Commun.* **2019**, *10*, 900.
[49] T. Ortmann, S. Burkhardt, J. K. Eckhardt, T. Fuchs, Z. Ding, J. Sann, M. Rohnke, Q. Ma, F. Tietz, D. Fattakhova-Rohlfing, C. Kübel, O. Guillon, C. Heiliger, J. Janek, *Adv. Energy Mater.* **2022**, https://doi.org/10.1002/aenm.202202712.
[50] M. J. Wang, E. Carmona, A. Gupta, P. Albertus, J. Sakamoto, *Nat. Commun.* **2020**, *11*, 5201.
[51] R. Murugan, V. Thangadurai, W. Weppner, *Angew. Chem., Int. Ed.* **2007**, *46*, 7778.
[52] Y. Zhu, J. G. Connell, S. Tepavcevic, P. Zapol, R. Garcia-Mendez, N. J. Taylor, J. Sakamoto, B. J. Ingram, L. A. Curtiss, J. W. Freeland, D. D. Fong, N. M. Markovic, *Adv. Energy Mater.* **2019**, *9*, 1803440.
[53] J. G. Connell, T. Fuchs, H. Hartmann, T. Krauskopf, Y. Zhu, J. Sann, G.-R. Mendez, J. Sakamoto, S. Tepavcevic, J. Janek, *Chem. Mater.* **2020**, *32*, 10207.
[54] Y. Zhu, X. He, Y. Mo, *ACS Appl. Mater. Interfaces* **2015**, *7*, 23685.
[55] T. Fuchs, C. G. Haslam, A. C. Moy, C. Lerch, T. Krauskopf, J. Sakamoto, F. H. Richter, J. Janek, *Adv. Energy Mater.* **2022**, 2201125.
[56] D. K. Singh, T. Fuchs, C. Krempaszky, B. Mogwitz, S. Burkhardt, F. H. Richter, J. Janek, *Adv. Funct. Mater.* **2023**, *33*, 2211067.
[57] S.-K. Otto, T. Fuchs, Y. Moryson, C. Lerch, B. Mogwitz, J. Sann, J. Janek, A. Henss, *ACS Appl. Energy Mater.* **2021**, *4*, 12798.
[58] A. Sharafi, E. Kazyak, A. L. Davis, S. Yu, T. Thompson, D. J. Siegel, N. P. Dasgupta, J. Sakamoto, *Chem. Mater.* **2017**, *29*, 7961.
[59] J. Gao, X. Guo, Y. Li, Z. Ma, X. Guo, H. Li, Y. Zhu, W. Zhou, *Adv. Theory Simul.* **2019**, *2*, 1900028.
[60] H. Koshikawa, S. Matsuda, K. Kamiya, M. Miyayama, Y. Kubo, K. Uosaki, K. Hashimoto, S. Nakanishi, *J. Power Sources* **2018**, *376*, 147.
[61] F. Yonemoto, A. Nishimura, M. Motoyama, N. Tsuchimine, S. Kobayashi, Y. Iriyama, *J. Power Sources* **2017**, *343*, 207.
[62] A. Badran, T. Clemenceau, N. Andriamady, D. Marshall, R. Raj, *MRS Commun.* **2021**, *11*, 283.
[63] T. Krauskopf, R. Dippel, H. Hartmann, K. Peppler, B. Mogwitz, F. H. Richter, W. G. Zeier, J. Janek, *Joule* **2019**, *3*, 2030.
[64] C. Lee, S. Y. Han, J. A. Lewis, P. P. Shetty, D. Yeh, Y. Liu, E. Klein, H.-W. Lee, M. T. McDowell, *ACS Energy Lett.* **2021**, *6*, 3261.
[65] K. Lee, E. Kazyak, M. J. Wang, N. P. Dasgupta, J. Sakamoto, *Joule* **2022**, *6*, 2547.
[66] F. Flatscher, M. Philipp, S. Ganschow, H. M. R. Wilkening, D. Rettenwander, *J. Mater. Chem. A* **2020**, *8*, 15782.
[67] T. Fuchs, J. Becker, C. G. Haslam, C. Lerch, J. Sakamoto, F. H. Richter, J. Janek, *Adv. Energy Mater.* **2022**, *13*, 2203174.
[68] T. Krauskopf, B. Mogwitz, C. Rosenbach, W. G. Zeier, J. Janek, *Adv. Energy Mater.* **2019**, *9*, 1902568.